ASSESSING EFFECTIVE MEDIUM THEORIES FOR DESIGNING COMPOSITES FOR NONLINEAR TRANSMISSION LINES

by

Xiaojun Zhu

A Thesis

Submitted to the Faculty of Purdue University

In Partial Fulfillment of the Requirements for the degree of

Master of Science in Nuclear Engineering

School of Nuclear Engineering

West Lafayette, Indiana

December 2019

THE PURDUE UNIVERSITY GRADUATE SCHOOL
STATEMENT OF COMMITTEE APPROVAL

Dr. Allen L. Garner, Chair
School of Nuclear Engineering

Dr. Robert S. Bean
School of Nuclear Engineering

Dr. Tyler N. Tallman
School of Aeronautics and Astronautics

Approved by:
Dr. Shripad Revankar
Head of the Graduate Program

To my families, who always support me.

ACKNOWLEDGMENTS

I would like to thank my advisor, Prof. Allen Garner, for his continuous support and guidance of my graduate study, research and writing this thesis, for his enthusiasm, motivation and patience. I am also very grateful to his guidance about academic career and life, it means a lot to me. I would like to thank Andrew Fairbanks for his countless support and advice in research and surely for his sense of humor. Furthermore, I would like to thank Nancy Isner, Agni Dhanabal, Russell Brayfield, Travis Crawford and many fellow students in the BioElectrics and ElectroPhysics (BEEP) for helping and supporting me in many ways. I would like to thank Weirong, Nathan and Matt, my friends and roommates, for the enjoyable moments and jokes they made, and for the generous help and quite nights they provided. I would like to thank my families for everything they have done for me. I would like to thank Siyu for her constant support and love.

I also acknowledge the Office of Naval Research (ONR) for funding this work under Grant Number N00014-18-1-2341.

.

TABLE OF CONTENTS

LIST OF TABLES

LIST OF FIGURES

ABSTRACT

Nonlinear transmission lines (NLTLs) are of great interest for high power microwave (HPM) generation because they can sharpen pulses to create an electromagnetic shockwave to produce oscillations from 100 MHz to low GHz. NLTLs provide frequency agility, compactness, durability and reliability, providing a solid-state radiofrequency (RF) source for producing HPM. The essential component of NLTLs is the nonlinear material, typically a dielectric that varies with voltage or a magnetic material whose permeability varies with current, incorporated in the transmission line in various topologies. This thesis presents an alternative approach involving designing composites comprised of nonlinear dielectric inclusions (barium strontium titanate (BST)) and/or nonlinear inductive inclusions (nickel zinc ferrites (NZF)) in a polymer base host material, analogous to electromagnetic interference designs that incorporate stainless steel inclusions of various shapes in a plastic to tune the composite's electromagnetic properties at GHz. Appropriately designing NLTL composites requires predicting these effective properties both in linear (for a fixed and low voltage and current) and nonlinear regions (permittivity and permeability become voltage dependent and current dependent, respectively) prior to designing HPM systems comprised of them. As a first step, this thesis evaluates and benchmarks composites models in the commercial software CST Microwave Studios (CST MWS) to various effective medium theories (EMTs) to predict the permittivity and permeability of composites of BST and/or NZF inclusions in the linear regime, compared with experimental measurements. The manufacturing and measurement of the nonlinear composites will be briefly discussed with an analysis of the homogeneity of a composite sample using 3D X-ray scan. Long-term

application of these approaches to predicting the effective nonlinear composite permittivity and permeability and future work will be discussed.

1. INTRODUCTION

1.1. Nonlinear transmission lines

Nonlinear transmission lines (NLTLs) have been used for high-power microwave (HPM) generation [1]–[5] and pulse sharpening [6] at frequencies ranging from 100 MHz to low GHz in recent decades. NLTLs provide multiple advantages, such as tunability, compactness and durability. In addition, NLTLs can be used as a solid-state RF sources with more reliability, providing inexpensive construction and less power consumption [5].

Here, we consider two NLTL topologies: (1) lumped element circuits (LEC) with nonlinear capacitors and/or inductors and (2) distributed transmission lines using nonlinear materials, focusing on gyromagnetic lines. Each design has its own advantages and disadvantages for NLTL design, study, or applications. The following sections outline the fundamentals of NLTLs for pulse sharpening and microwave generation. The mechanism for microwave generation of gyromagnetic lines and hybrid lines will be introduced separately for the interest of our work.

1.1.1. The fundamental of NLTLs

The essential component of NLTLs is the nonlinear material, which causes the dielectric properties to vary with voltage or the magnetic properties to vary with current. From a lumped element perspective, one may induce this nonlinearity with nonlinear capacitors and/or inductors, as shown in Figure 1, or by a transmission line composed of a nonlinear material, such as a ferrite loaded coaxial line, forming a gyromagnetic line [1], [7] in Figure

2. Ferroelectric and ferromagnetic materials can provide nonlinearity and tunability in NLTLs, meaning that the electric polarization or magnetization varies under an applied external electric or magnetic field. Thus, the permittivity or permeability may be voltage- or current dependent and current-dependent for ferroelectric or ferromagnetic materials, respectively.

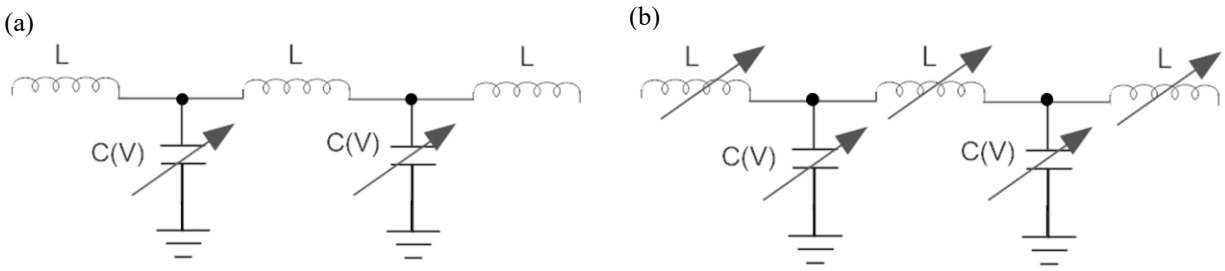

Figure 1. (a) 1D NLTL with nonlinear capacitors. (b). A hybrid NLTL with nonlinear capacitors and nonlinear inductors © 2018 IEEE [8].

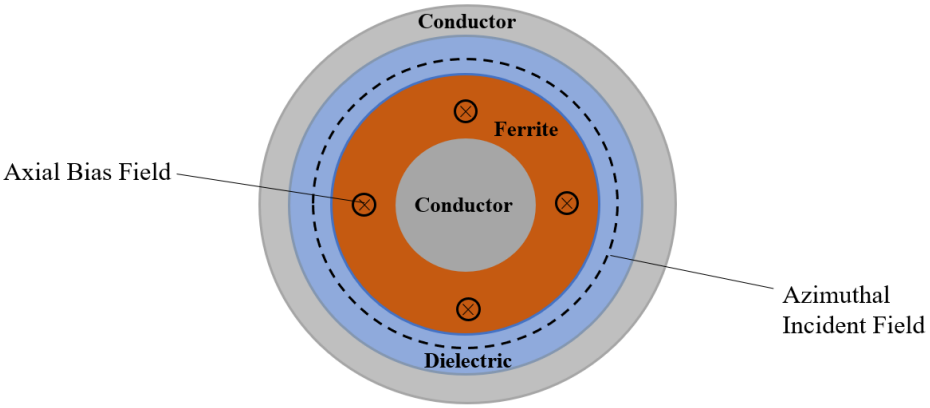

Figure 2. A cross-sectional view of the gyromagnetic NLTL with conductors, dielectric, ferrite and magnetic fields © 2013 IEEE [1]

Pulse sharpening occurs due to the permittivity and permeability of the nonlinear materials changing as the electromagnetic wave propagates through a NLTL. The permittivity and/or

permeability of nonlinear materials decreases with increasing voltage and/or current, yielding different phase velocities $v_p = [\varepsilon(V)\mu(I)]^{-1/2}$, where ε is permittivity, μ is permeability, V is voltage, and I is current, for different propagating pulse portions. The pulse peak with a higher electric/magnetic field magnitude propagates faster than the portion with lower field magnitude, such as the leading edge. Thus, the peak of the pulse will catch up to the leading edge, reducing the pulse rise time, and forming a shock wave. Figure 3 illustrates that a gradual line containing of several segments is used to gradually reduce the pulse width of the input pulse [6].

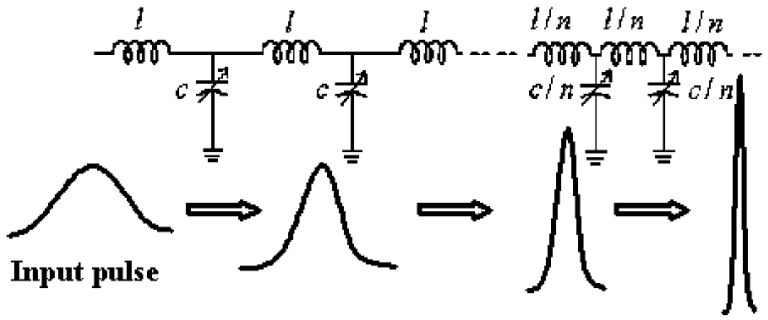

Figure 3. Schematic of the gradually scaled NLTL © 2005 IEEE [6].

The following example illustrates the mechanism of oscillation formation, or the transition from pulse sharpening to microwave generation. For a nonlinear dispersive lumped element transmission line, if the input pulse has a rise time t_{ri} on the order of $1/f_c$, where f_c is the Bragg cutoff frequency [3], [9]–[11], given by

$$f_c = \frac{1}{\pi\sqrt{LC(V_{max})}} \tag{1}$$

where V_{max} is the maximum voltage for the input pulse, L is the inductance, and C is the

capacitance, the reduction of the output pulse rise time or the shock wave front will be restrained by the Bragg cutoff frequency. Because the steepness of the shock wave front cannot be infinite and is ultimately limited by the relaxation time of the nonlinear materials [10]. Additionally, the frequencies of the narrow pulses or shock wave f_s are limited by the Bragg cutoff frequency ($f_s < f_c$), yielding an array of solitons to form an oscillation at the output [3], [10]–[13], as shown in Figure 3. A typical operating f_s is determined by $f_s \approx f_c/2$ [3].

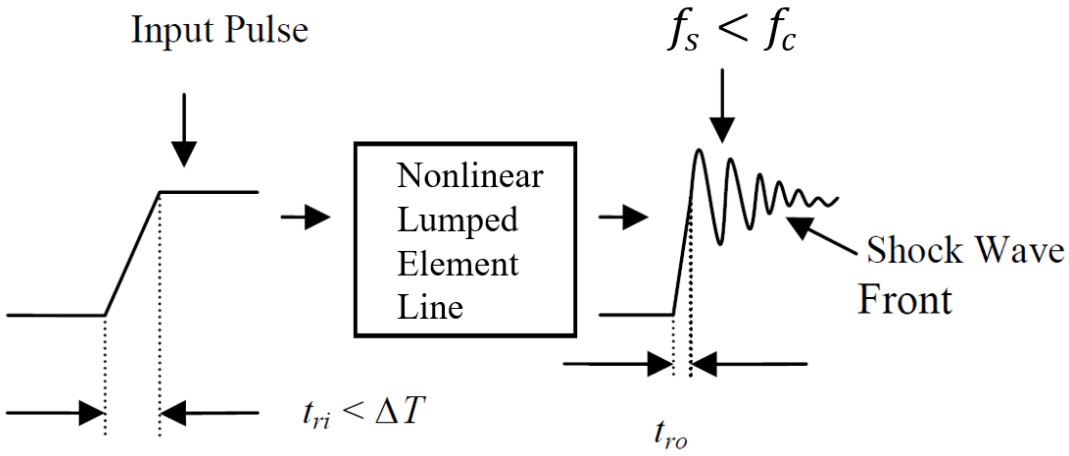

Figure 4. An oscillation burst of solitons produced in an LC ladder © 2009 IEEE [10].

Alternatively, one may use a ferrite in a coaxial transmission line with a bias magnetic field, as shown in Figure 2. This is based on damped gyromagnetic precession, and further details will be introduced in the gyromagnetic lines section.

1.1.2. Lumped element circuits NLTLs

LEC NLTLs are more amenable to mathematically studying the impact of nonlinear capacitance and inductance on electromagnetic wave transmission since the circuit equations are straightforward to solve and it is experimentally convenient to design systems

comprised of nonlinear capacitors and/or inductors. Mathematical models are well established for demonstrating pulse sharpening for these scenarios. For instance, the circuit equation for a NLTL with nonlinear capacitance $C(V)$ and linear inductance assuming $V_n(t) \approx V(x,t)$ is given by [14]

$$L\frac{\partial^2 C(V)V}{\partial t^2} = \frac{\partial^2 V}{\partial x^2} + \frac{\delta^2}{12}\frac{\partial^4 V}{\partial x^4}, \tag{2}$$

where δ is the length of each segment of the NLTL, L is the inductance, C is the capacitance, V is the voltage, and n represents the n^{th} node of the transmission line. A first-order linear approximation to the nonlinear capacitance gives [6]

$$C(V) = C_0(1 - bV), \tag{3}$$

where b and C_0 are constants. Combining (2) and (3) suggests that achieving large-amplitude narrow pulses requires that the capacitance and/or inductance of the LEC NLTLs must vary as much as possible and the nonlinearity factor b must be sufficiently large to compensate for the dispersion. Alternatively, one may use a positive voltage-dependent capacitor, such as a MOS varactor, for edge sharpening and possibly for digital transmission [6]. Ref. [6] showed that accumulation-mode MOS varactors induced considerable edge sharpening of both rise and fall times. This study also applied a gradual scaling technique for both L and C, letting their ratio to be constant for each segment to avoid reflections [6]. Numerical methods, such as the Runge-Kutta method [14], and commercial software, such as COMSOL [15] and SPICE [16], have been used to solve the mathematical models of LEC NLTLs for design optimization and elucidate the physics involved.

Experiments using LEC NLTLs with commercial-off-the-shelf (COTS) components agree well with circuit models [17]. Both experiments and simulations show that placing the load across the inductor in the last section of the NLTLs significantly increases oscillation amplitudes and efficiency compared to conventional NLTLs [17]. The LEC nonlinear capacitive line (NLCL) using commercial-off-the-shelf (COTS) components can generate HPM with peak power of tens of MW in agreement with a mathematical model applying a hyperbolic tangent function with two fitting parameters to represent the nonlinearity of the barium titanate ceramic capacitors [18].

BAE Systems designed another type of NLTL called the nonlinear inductive line (NLIL) using nonlinear inductors to achieved 20 MW at 1 GHz with a repetition rate of 1-1.5 kHz and tunability of 20% [19]. However, LEC NLILs are relatively long, with typical lengths of approximately 6 m [19]. LEC NLTLs have limited reliability because the whole system fails if a single component malfunctions. Moreover, using varactors in these designs introduces significant challenges since varactors are low voltage devices susceptible to either damage or loss of nonlinearity at higher voltages and provide limited frequency agility since a given varactors device frequency is not tunable

1.1.3. Gyromagnetic lines

Another NLTL topology uses coaxial or parallel plate geometries with nonlinear materials. Figure 2 shows a ferrite-filled coaxial geometry referred to as a gyromagnetic line, which is generally biased by an external magnetic field [1], [19]–[25]. The biased field may be applied using various permanent magnet configurations [19] or a solenoid wrapped around

the transmission lines [22]. The coherent precession of the magnetic moment is desirable for maximizing microwave power. When a pulse is applied in a gyromagnetic line, with the bias field the ferrite is much easier to saturate, allowing more magnetic moments to precess around the effective magnetic field [25]. This will induce damped gyromagnetic precession, yielding high frequency voltage oscillations on the pulse front for HPM generation [3]. The processional motion of magnetization can be mathematically determined by the Landau-Lifshitz-Gilbert (LLG) equation [26], [27], given by

$$\frac{\partial \boldsymbol{m}}{\partial t} = -\gamma \boldsymbol{m} \times \boldsymbol{H}_{eff} + \alpha \boldsymbol{m} \times \frac{\partial \boldsymbol{m}}{\partial t} \tag{4}$$

where $\boldsymbol{m}$ is the normalized magnetization, $\boldsymbol{H}_{eff}$ is the effective magnetic field, γ is the gyromagnetic ratio, and α is the damping constant, which remains unknown and assumed to be 0.01-1 and dependent on loaded materials. Figure 5 graphically describes the LLG equation [1].

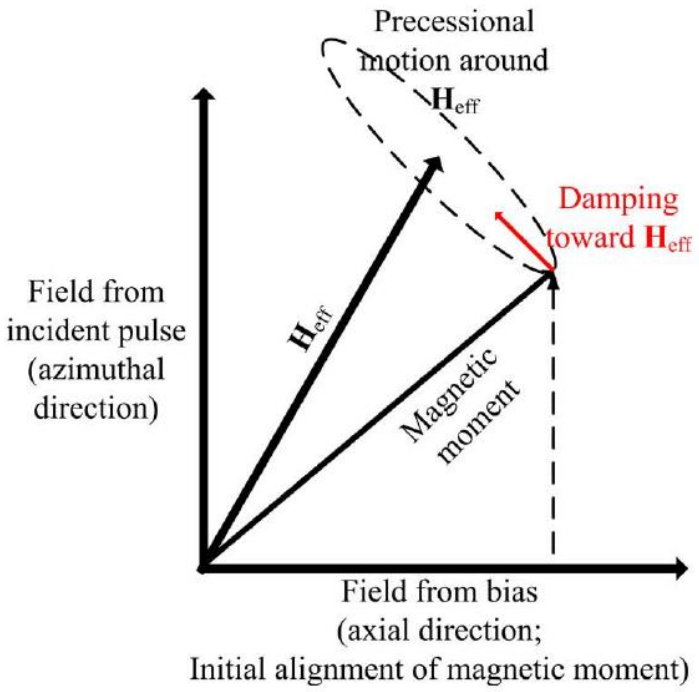

Figure 5. A vector representation of the magnetization dynamics © 2013 IEEE [1].

Applying the input pulse to the line causes the ferrites to reach saturation, sharpening the pulses. Simultaneously the magnetization $\boldsymbol{m}$ precesses around the effective magnetic field $\boldsymbol{H}_{eff}$, described by the first term on the right-hand side (RHS) of (4). With a damping effect, represented by the second term on the RHS, the magnetization performs damping precession around $\boldsymbol{H}_{eff}$ and will finally align in the direction of $\boldsymbol{H}_{eff}$ [27].

Gyromagnetic NLTLs generate peak RF powers of hundreds of MW with a central frequency of approximately 1 GHz [20], [21]. Recently, gyromagnetic NLTLs applying simultaneous axial and azimuthal biases show that the azimuthal bias has a direct relation with the modulation and compression of the output pulses, obtaining a relatively higher efficiency of 20% compared with the efficiency of 10% for most LEC NLTLs [23]. The gyromagnetic NLTLs exhibit strong tunability and relatively high peak power and

efficiency. However, corona discharges can limit the operating voltage for gyromagnetic lines [28].

1.1.4. Hybrid NLTLs

Parallel plate NLTLs using nonlinear ceramic dielectric slabs also have been used for soliton and RF generation [29]–[32]. NLTLs combining ferrites and nonlinear ceramic dielectric for inducing nonlinear permeability and permittivity, respectively, are referred to as hybrid lines (NLHLs). The idea was first proposed for pulse sharpening since it facilitates load matching by simultaneously selecting both $L(I)$ and $C(V)$ during pulse sharpening by appropriately choosing the functions [33]. For an NLHL, the circuit equation can be written in a more general form compared than (2), given by [34]

$$\frac{\partial}{\partial t}\left[L(I)C(V)\frac{\partial V}{\partial t}\right] = \frac{\partial^2 V}{\partial x^2} + \frac{\delta^2}{12}\frac{\partial^4 V}{\partial x^4} \tag{5}$$

with a first-order linear approximation for nonlinear inductance anlogous to (3) as

$$L(I) = L_0(1 - dI) \tag{6}$$

where d is the nonlinearity factor for the inductance. A theoretical study demonstrated that an NLHL could increase compression of the output pulse [3], [35]. Another circuit simulation suggest that NLHLs have the potential to generate pulses with greater oscillation amplitudes and higher frequency and greater frequency tunability by applying bias circuits to the nonlinear components at low voltages [32]. A subsequent study at high voltages showed an unmatched NLHL can also generate RF oscillations [36], albeit with

reduced voltage modulation depth. An experiment of NLHLs using COTS ceramic capacitors and commercial ferrite bead inductors showed that NLHLs may achieve RF in the MHz range with higher voltage modulation depth compared with non-hybrid lines due to stronger nonlinearity [8].

1.2. Motivation and thesis layout

This thesis evaluates and explores the feasibility of novel composites comprised of a polymer filled with nonlinear dielectric or magnetic inclusions to tune NLTL properties for ultimate HPM applications. One may tune the effective permittivity and permeability of the composite by varying the volume loading of the nonlinear dielectric inclusions (e.g. barium strontium titanate (BST)) and nonlinear magnetic inclusions (e.g. nickel zinc ferrites (NZF)) or altering the inclusion shape (e.g. spheres, flakes, or fibers). This is analogous to electromagnetic interference designs that incorporate stainless steel inclusions of various shapes in a plastic to tune the composite's electromagnetic properties at GHz [37].

Appropriately designing NLTL composites requires predicting these effective properties and, ultimately, designing the HPM systems using them. As a first step, this thesis benchmarks various effective medium theories (EMTs) to predict the permittivity and permeability of various composites of BST and/or NZF inclusions in the linear regime (for a fixed low voltage and current).

We first apply EMTs to predict AC measurements of permeability and permittivity for composites comprised of a polymer with BST and/or NZF spheres. We describe preliminary studies applying CST Microwave Studio (CST MWS) to predict the effective permittivity and permeability of these composites and compare the results to experiments and EMTs. Benchmarking the CST MWS simulations with the measurements will ultimately permit efficient assessment of the influence of the inclusion shape, orientation (for non-spherical shape), electromagnetic wave propagation, and various EMTs. Additionally, CST MWS provides the capability to introduce nonlinear dielectric and magnetic properties and ultimately couple the knowledge of composite properties into a full HPM system model using a single software.

The remainder of this thesis will proceed as follows. Chapter 2 provides the background of the dielectric properties, effective medium theories (EMTs) and their limitations, and simulation approaches for determining composite effective properties. Chapter 3 briefly introduces the manufacturing procedures of BST, NZF and BST/NZF composites, the assessment of composite homogeneity using a 3D X-ray Microscope, and measurement of composite dielectric properties in the linear regime. Chapter 4 compares dielectric properties from the literature values and our fits of experimental data for BST and NZF and uses them as inputs for CST MWS composite models. Chapter 4 also summarizes the CST MWS procedure. Chapter 5 compares results for BST, NZF and BST/NZF composite simulations to measurements. Chapter 6 discusses future work for improving the present models and predicting the effective nonlinear composite permittivity and permeability.

2. BACKGROUND

Many composite designs aim to achieve desired electrical and mechanical effective properties [38]. There are two main approaches for determining the effective properties of composites: effective medium theories (EMTs) [38]–[42] and computational methods [43]–[46]. EMTs, also called mixing rules, have been derived to predict the effective properties of composites for mechanical and electrical applications, such as elastic metamaterials [39], electromagnetic shielding, radar absorption, electromagnetic compatibility [40]. On the other hand, various numerical simulations have been developed for determining the effective properties for composites or metamaterials with great success [41], [47], [48]. Before examining these theories or simulations for the effective dielectric properties, we first introduce the physics behind dielectric properties.

2.1. The Fundamental of Dielectric Properties

2.1.1. Polarization

Unlike conductors, dielectric materials would not conduct electricity when exposed to an external electrical field [42]. Instead, the permanent or induced electrical dipole moments in dielectrics would allow the dielectrics to be polarized by the external field so that they can store electrical energy persistently or transiently. The polarization density $\boldsymbol{P}$, or simply polarization, represents the density of these dipole moments and is given by

$$\boldsymbol{P} = \frac{d\boldsymbol{p}}{dV} \tag{7}$$

where $\boldsymbol{p}$ is the dipole moment and dV is the volume element. For magnetic materials,

one can write an analogous formula for magnetization $\boldsymbol{M}$, also called magnetic polarization, as

$$\boldsymbol{M} = \frac{d\boldsymbol{m}}{dV} \tag{8}$$

where $\boldsymbol{m}$ is the permanent or induced magnetic dipole moment induced by the spin of the electrons or the external current (magnetic field), respectively. Generally, without the external field, the permanent dipole moments or permanent magnetic moments are randomly oriented due to thermal motion, exhibiting no polarization or magnetization.

Under an alternating electric field, the electrical polarization mechanisms may be classified into orientational, atomic and ionic, electronic and interfacial polarization for different frequencies [42]. Each mechanism responds to a specific frequency range or occurs for certain materials. For example, the electronic polarization occurs at optical and ultraviolet frequencies, while the atomic polarization responds at optical and infrared frequencies. Both mechanisms are resonant behaviors. At microwave frequencies, the orientational (dipolar) polarization occurs when the external field exerts a torque on a dipole moment, and the dipole moment will rotate to align with the field, resulting in orientational polarization. For a matter that is not completely lossless, the rotation of the dipole will induce a friction to contribute to the dielectric losses [49], [50].

2.1.2. Complex permittivity and permeability

For microwave applications, materials are generally characterized by real permittivity (permeability) and loss tangent (magnetic loss tangent) and may be written as complex

permittivity (permeability). Here, we connect these quantities with polarization mentioned above. Maxwell's equations for electric and magnetic field in differential form are given by [49]

$$\nabla \times \boldsymbol{E} = -j\omega \boldsymbol{B} \tag{9}$$

$$\nabla \times \boldsymbol{H} = j\omega \boldsymbol{D} + \boldsymbol{J} \tag{10}$$

respectively, where

$$\boldsymbol{D} = \varepsilon_0 \boldsymbol{E} + \boldsymbol{P} \tag{11}$$

$$\boldsymbol{B} = \mu_0 (\boldsymbol{H} + \boldsymbol{M}) \tag{12}$$

with

$\boldsymbol{E}$ = electric field [V/m]

$\boldsymbol{H}$ = magnetic field [A/m]

$\boldsymbol{D}$ = electric flux density or displacement flux [$A \cdot s/m^2$]

$\boldsymbol{B}$ = magnetic flux density [$V \cdot s/m^2$]

$\boldsymbol{J}$ = electrical current density [A/m^2]

$\varepsilon_0 \cong 8.854 \times 10^{-12}$ F/m = permittivity of free space

$\mu_0 \cong 1.256 \times 10^{-6}$ H/m = permeability of free space

ω = angular frequency

For a dielectric material, the polarization $\boldsymbol{P}$ induced by the external field increases the total displacement flux $\boldsymbol{D}$, as shown in (11), analogous to the magnetization increases the magnetic flux density $\boldsymbol{B}$ in (12). If the dielectric material is linear the polarization will be linearly related to the field by

$$\boldsymbol{P} = \varepsilon_0 \chi_e \boldsymbol{E} \tag{13}$$

$$\boldsymbol{M} = \mu_0 \chi_m \boldsymbol{H} \tag{14}$$

where χ_e is the electric susceptibility and χ_m represents the magnetic susceptibility. Using Ohm's law $\boldsymbol{J} = \sigma \boldsymbol{E}$ and complex permittivity $\varepsilon = \varepsilon' - j\varepsilon'' = \varepsilon_0(1 + \chi_e)$, (10) can be written as

$$\nabla \times \boldsymbol{H} = j\omega(\varepsilon' - j\varepsilon'' - j\frac{\sigma}{\omega})\boldsymbol{E} \tag{15}$$

where σ is the conductivity of the material. The term $\omega\varepsilon'' + \sigma$ contributes to the dielectric loss and can be considered as the total effective conductivity [49]. If σ is negligible compared with the loss from the dipole moment rotation $\omega\varepsilon''$, the loss tangent is given by

$$\tan\delta = \frac{\omega\varepsilon'' + \sigma}{\omega\varepsilon'} \cong \frac{\varepsilon''}{\varepsilon'} \tag{16}$$

where $\varepsilon' = \varepsilon_r'\varepsilon_0$ and $\varepsilon'' = \varepsilon_r''\varepsilon_0$ are the real and imaginary component of the complex permittivity (the relative permittivity $\varepsilon_r = \varepsilon_r' - j\varepsilon_r''$), respectively. For the complex permittivity ε, the imaginary part of ε must be negative ($\varepsilon'' > 0$) due to energy conservation [49]. An analogous consideration for (9) can be written as

$$\nabla \times \boldsymbol{E} = -j\omega(\mu' - j\mu'')\boldsymbol{H} \tag{17}$$

where $\mu' - j\mu'' = \mu$ is the complex permeability and μ'' represents the loss due to the damping of magnetic dipole moments. The magnetic loss tangent is given by

$$\tan \delta_m = \frac{\mu''}{\mu'}. \quad (18)$$

Generally, there is no magnetic conductivity because we did not consider the (fictitious) magnetic current density in (9). Additionally, the relative permeability can be written as $\mu_r = (\mu' - j\mu'')/\mu_0 = \mu_r' - j\mu_r''$.

2.1.3. Dispersion and relaxation

As mentioned above, polarization and magnetization strongly depend on the frequency of the field. Thus, the real and imaginary parts of the permittivity and permeability are frequency dependent. This dependence is called as dispersion [42], [51]. Figure 6 shows typical dispersion curves for the real and imaginary permittivity with different types of polarization mechanisms [42].

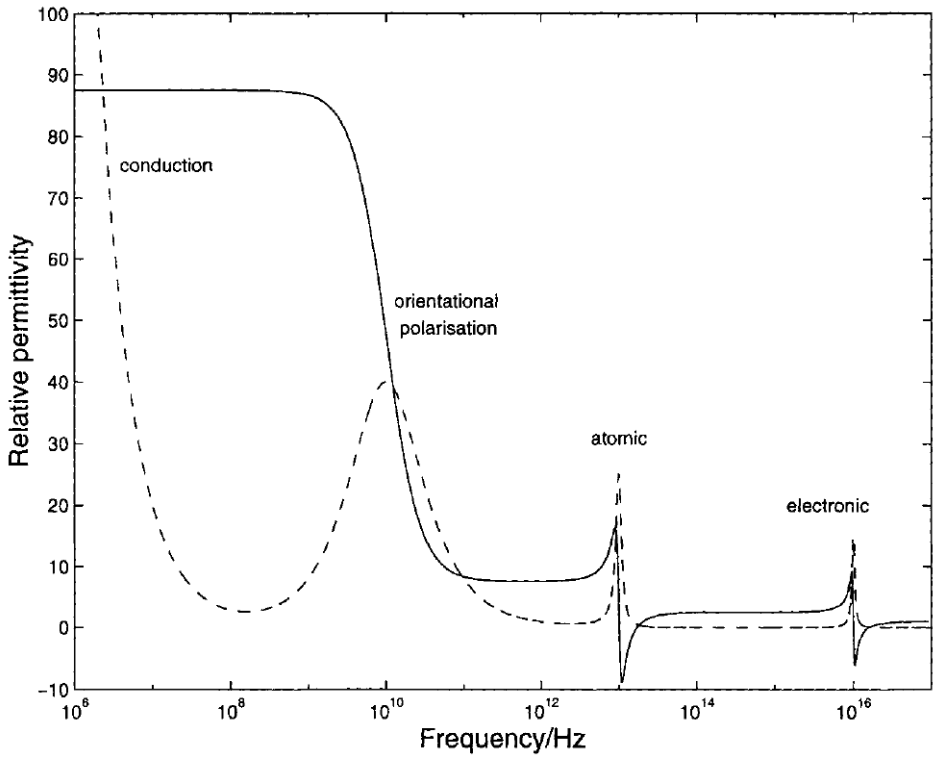

Figure 6. The dependence of the real (solid line) and imaginary (dashed line) permittivity of a material with various polarization mechanisms. Reproduced with permission from *Electromagnetic Mixing Formulas and Applications, Ari Sihvola* published by The Institution of Engineering and Technology, *1999*, DOI: 10.1049/PBEW047E [42].

Around the microwave frequency range corresponding to the orientational polarization, the dispersion curve shows a peak of the imaginary part of permittivity with a drop of the real part of permittivity. This variation of the complex permittivity is due to the mobility of the dipoles which can be described by the relaxation time τ or relaxation frequency f_r with $\tau = 1/(2\pi f_r)$. The relaxation time is the time required for a dipole moment to align with the field [50]. At low frequencies the field variation is slow, allowing the dipoles to keep pace with the varying field so that the orientational polarization can fully develop before the field changes its direction. Thus, ε' is almost constant before the drop, while ε'' is proportional to the frequency due to the friction of varying dipoles. As the higher frequency, ε' decrease because of the phase lag between the dipoles and the electric field. At

frequencies above f_r, the field variation becomes faster with increasing frequency, resulting in less effect on the rotation of dipole moments, and thus both real and imaginary part of permittivity decrease [50].

Ferrites, such as NiZn or MnZn ferrites, have permeability spectra characterized by different dispersion mechanisms: gyromagnetic spin rotation, domain-wall motion, and magnetization rotation [51], [52]. Generally, at RF, the first two mechanisms give a resonance-type frequency dispersion and the third one has a relaxation-type dispersion. For NiZn ferrites ($Ni_{0.24}Zn_{0.65}Fe_{2.04}O_4$), the complex permeability spectrum can be treated by the superposition of the dispersions with different mechanisms [51]. For materials with relatively high conductivity such as MnZn ferrites, the eddy current loss must be considered in permeability spectra. However, one can ignore the eddy current effect in MnZn ferrite composites mixing with binder matrix because of the increase of the resistivity of the composites [51], [53].

2.2. Effective Medium Theories

Although EMTs were originally derived to predict the effective permittivity of mixtures, certain universality from the dielectric homogenization theories allow an EMT equally valid and applicable for other effective properties, such as the effective magnetic permeability, electric conductivity, thermal conductivity, particle diffusivity, and certain elastic properties [42]. For randomly oriented anisotropic inclusions, the mixture can be considered isotropic [42], [54]. In addition, inclusions are generally assumed to be randomly and homogeneously distributed.

2.2.1. Classical EMTs

Classical EMTs, such as Maxwell-Garnett (MG) formula [55], Bruggeman rule (BR) [56] and coherent potential (CP) formula are physically based and have been widely used in electromagnetics literature for suspensions of spheres and ellipsoids [42], [57], [58], as summarized in Table. 1. The MG formula can be derived from the average fields, the coherent potential formula came from the theoretical studies of wave propagation in random media [42], [59]. Here, we will briefly introduce the derivation of the MG rule from an average static field perspective. For an electrostatic field applied to a two-phase mixture, using (11) and (13) gives the effective permittivity of the mixture ε_{eff} as:

$$\langle \boldsymbol{D} \rangle = \varepsilon_{eff} \langle \boldsymbol{E} \rangle \tag{19}$$

where $\langle \boldsymbol{D} \rangle$ and $\langle \boldsymbol{E} \rangle$ are the volume-averaged flux density and electric field [42], respectively. The average flux density and electric field with the corresponding volume loadings of each phase are

$$\langle \boldsymbol{D} \rangle = \varepsilon_i f \boldsymbol{E}_i + (1-f)\varepsilon_e \boldsymbol{E}_e \tag{20}$$

and

$$\langle \boldsymbol{E} \rangle = f \boldsymbol{E}_i + (1-f)\boldsymbol{E}_e \tag{21}$$

respectively, where ε_e and ε_i represent the permittivity for the host and the inclusion, respectively, and f is the volume loading of the inclusions. Assuming $\boldsymbol{E}_e$ and ε_i constant gives the effective permittivity can be written as [42]

$$\varepsilon_{eff} = \frac{f\varepsilon_i A + \varepsilon_e(1-f)}{fA + (1-f)} \tag{22}$$

where A is the field ratio $\boldsymbol{E}_i = A\boldsymbol{E}_e$. Defining $A = 3\varepsilon_e/(\varepsilon_i + 2\varepsilon_e)$ for spheres [42] yields

$$\varepsilon_{eff} = \varepsilon_e + 3f\varepsilon_e \frac{\varepsilon_i - \varepsilon_e}{\varepsilon_i + 2\varepsilon_e - f(\varepsilon_i - \varepsilon_e)} \tag{23}$$

for the MG rule. Here, A for spheres may be derived from the field analysis of a dielectric sphere surrounded by a dipole field perturbation caused by a uniform field. One may also derive the MG formula from the Clausius-Mossotti formula by applying the Lorentz local field with the depolarization factor of a sphere [42]. Ref. [59] provides additional derivation details.

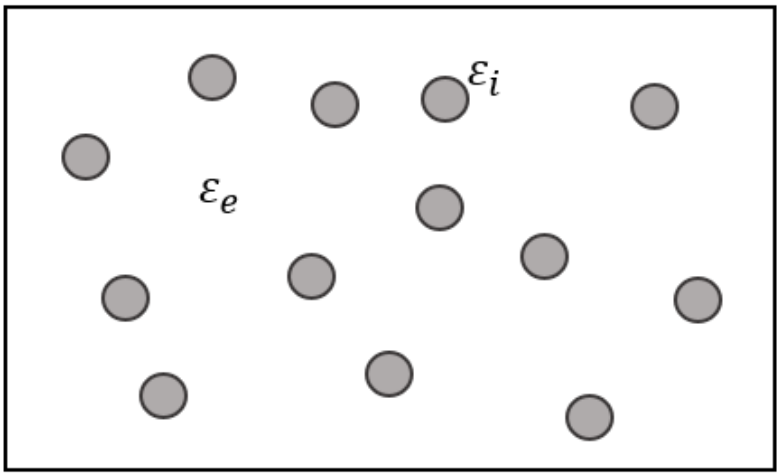

Figure 7. Randomly distributed spherical inclusions as guests in the dielectric host material, forming a two-phase mixture.

The Looyenga (LO) [60] and Lichtenecker (LI) [61] mixing formulae were derived by differential analysis, as given in Table 1 [54]. A recent study derived the LI formula from Maxwell's equations and charge conservation to a composite with randomly distributed and randomly orientated particles [62].

Table 1. Classical EMTs for sphere inclusions with MG = Maxwell Garnett, BR = Bruggeman, CP = coherent potential, LO = Looyenga, LI = Lichtenecker [42], [55]–[58], [60], [61], [63].

$\varepsilon_{eff} = \varepsilon_e + 3f\varepsilon_e \frac{\varepsilon_i - \varepsilon_e}{\varepsilon_i + 2\varepsilon_e - f(\varepsilon_i - \varepsilon_e)}$	MG
$(1-f)\frac{\varepsilon_e - \varepsilon_{eff}}{\varepsilon_e + 2\varepsilon_{eff}} + f\frac{\varepsilon_i - \varepsilon_{eff}}{\varepsilon_i + 2\varepsilon_{eff}} = 0$	BR
$\varepsilon_{eff} = \varepsilon_e + f(\varepsilon_i - \varepsilon_e)\frac{3\varepsilon_{eff}}{3\varepsilon_{eff} + (1-f)(\varepsilon_i - \varepsilon_e)}$	CP
${\varepsilon_{eff}}^{1/3} = (1-f){\varepsilon_e}^{1/3} + f{\varepsilon_i}^{1/3}$	LO
$\log\varepsilon_{eff} = f\log\varepsilon_i + (1-f)\log\varepsilon_e$	LI
$\varepsilon_{eff} = \varepsilon_e + 3\varepsilon_e \frac{\sum_{k=1}^{K} f_i \frac{\varepsilon_k - \varepsilon_e}{\varepsilon_k + 2\varepsilon_e}}{1 - \sum_{k=1}^{K} f_k \frac{\varepsilon_k - \varepsilon_e}{\varepsilon_k + 2\varepsilon_e}}$	MG multiphase
$\varepsilon_{eff} = \prod_{k=1}^{K} \varepsilon_k^{f_k}$	LI multiphase

The first three mixing rules are valid for composites containing ellipsoidal inclusions by introducing the depolarization factors which are simplified for the application of spherical inclusions [42]. The orientations of non-spherical inclusions can greatly impact the effective properties of a mixture if the inclusions are not randomly orientated [42], [64]–[68]. In addition, classical EMTs may be applied for multiphase mixtures [42], [63], as summarized in Table 1, but those are not in the focus in this section.

2.2.2. Limitations of classical EMTs

The analysis and derivations above for classical EMTs were based on an electrostatic field. When treating an electromagnetic wave propagating through a mixture, classical EMTs are limited to inclusions with a sufficiently small size compared with the wavelength in the mixture so that the mixture may be considered as a homogeneous or effective medium. A quantitative criterion, called the quasi-static limit, is approximately given by [58]

$$\frac{\lambda}{2\pi} > \delta \tag{24}$$

where δ is the size of the inclusions and λ is wavelength in the mixture.

Classical EMTs are generally limited to cases where the volume loading of inclusions is low (dilute mixtures) or the electrical contrast is not too great [54]. For example, in the application of remote sensing, the contrast between the permittivity of different phases of the mixtures is not significant, thus both the MG and BR formals are able to predict the effective permittivity with good accuracy [54]. However, in other applications such as the composites mixed with a polymer host and metal inclusions, the electrical contrast between the phases might be very large [48]. Besides, the volume loadings of inclusions might vary from 10% to 80% [48]. Thus, one may apply alternative models for predicting the effective properties of such composites.

2.2.3. Generalized EMTs

The generalized EMTs (GEMTs) are semi-empirical approaches that have been developed by McLachlan [69] and other researchers [37], [38], [70]–[72] for a wide range of

frequency and volume loading. The GEMTs were derived from the physically based EMTs, such as MG or BR rules, by modifying the original rule with two fitting parameters. A typical BR rule based GEMT for a two-phase isotropic composite can be given by [70]

$$(1-f)\frac{{\varepsilon_e}^{1/s}-{\varepsilon_{eff}}^{1/s}}{{\varepsilon_e}^{1/s}+A{\varepsilon_{eff}}^{1/s}}+f\frac{{\varepsilon_i}^{1/t}-{\varepsilon_{eff}}^{1/t}}{{\varepsilon_i}^{1/t}+A{\varepsilon_{eff}}^{1/t}} \tag{25}$$

where s and t are fitting parameters, $A=(1-v_c)/v_c$ with v_c the percolation threshold. Each permittivity may be complex and may be replaced by conductivity or permeability. While there are some suggestions for the universality of s and t with $0.8<s<1$ and $t>1$ [71] or $1.5<t<2$ [70], obtaining an accurate predictive model for specific mixtures with certain shapes, electric properties of phases still requires determining these parameters (*s*, *t*, *A*) via measurements. A general procedure to define these parameters is to fit two of them by fixing one in the universal region, for example, with fixed $s=0.8$ *t* and *A* can be fitted through all frequency and volume loading of interest [38]. While such procedures can make the derived GEMT accurate for specific composites, the fitting work and necessary measurements are not trivial and their a priori capability (such as for a different inclusion material or shape) is unclear.

2.3. Simulation of Effective Dielectric Properties

It has been suggested that computer simulation may be the best solution for predicting the effective permittivity of mixtures [37], [73]. Sareni, et al. first presented a simulation approach for effective permittivity in the quasi-static limit based on the boundary integral equations and the finite element method, suggesting the limitations of standard analytical

models for composites with high volume loadings of the dispersed phase [74]. They subsequently assessed the impact of geometry, spatial arrangement, and the orientation of inclusions in a two-phase system with periodic lattices of inhomogeneities [74], [75].

Myroshnychenko and Brosseau developed a computer code to predict the effective permittivity for a system with a homogeneous host containing inhomogeneities of randomly oriented hard disks by applying a finite element description, an ordinary Monte Carlo sampling, and periodic boundary conditions [76]. They subsequently adapted this approach to predict the complex permittivity of a 2D two-phase statistically isotropic heterostructures in the quasi-static limit [77], [78]. Their results were compared with the GEMT to specifically determine the exponents s and t in (25) [37], [78], [79].

The next two sections will focus on the simulation approach using commercial software, such as COMSOL, CST EM studio, CST MWS studio, and relevant numerical methods.

2.3.1. Electrostatic models

Cooperating with various EMTs, simulations also have been developed for determining the effective dielectric properties of composites using commercial software. The electrostatic models are used in COMSOL Multiphysics and CST EM studio [43], [44] for determining the composite effective permittivity. By solving the three-dimensional Laplace equation to determine the potential and electric field, the relative effective permittivity of the composite can be calculated from [43]

$$\varepsilon_r = d\frac{\int D \cdot EdV}{\varepsilon_0 AU^2} \tag{26}$$

where D and E are the dielectric displacement and electric field, respectively, U is the applied voltage, d is the thickness of the sample, A is the area of the composite, as illustrated in Figure 8. The model in COMSOL shows that the effective permittivity is proportional to the size of the inclusions and the volume fraction, suggesting a rapid increase of the effective permittivity above percolation due to the increasing paths of the inclusions between the electrodes.

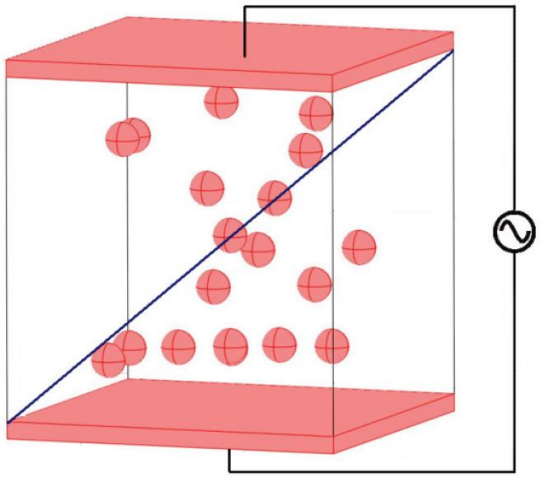

Figure 8. An illustration of the effective dielectric constant simulation using the electrostatic module of COMSOL © 2009 IEEE [43].

Two types of models (hard and soft) are applied for the filler and voids [43], [44]. Using hard spheres prevent overlaps of particles, standing for the inclusions, while soft spheres allow particle intersection that represents voids with more complex geometry. The results from the electrostatic model in CST EM agree well with the Lichtenecker (LI) rule for the composite with high electrical contrast for filler volume fraction from 5 to 50% [44]. Moreover, using CST EM Studio allows the visualization of the electric field distribution

within the composite and across the inclusions to assess dielectric failure of the composite [44].

2.3.2. Electromagnetic simulations

Rather than using electrostatic simulation, 3D electromagnetic simulations are applied in CST MWS [41], [45] to determine the effective complex permittivity and permeability from transmission (S_{21}) and reflection (S_{11}) characteristics of dielectric composites. After obtaining the *S*-parameters (S_{11} and S_{21}) of a slab of dielectric composite or metamaterial by simulation or measurement for a specific frequency range, methods exist to extract the effective refractive index n and impedance z [47], [80] from which one may calculate $\varepsilon_{eff} = n/z$ and $\mu_{eff} = nz$ [47], [80], [81].

Baer, et al. [45] applied the Baker-Jarvis method [80] to calculate the effective permittivity of the composite with low electric contrast at the microwave range with good agreement with the Maxwell-Garnett equation. Figure 9 summarizes the procedure which includes randomly generating particles, simulating in CST MWS, and calculating of the effective permittivity.

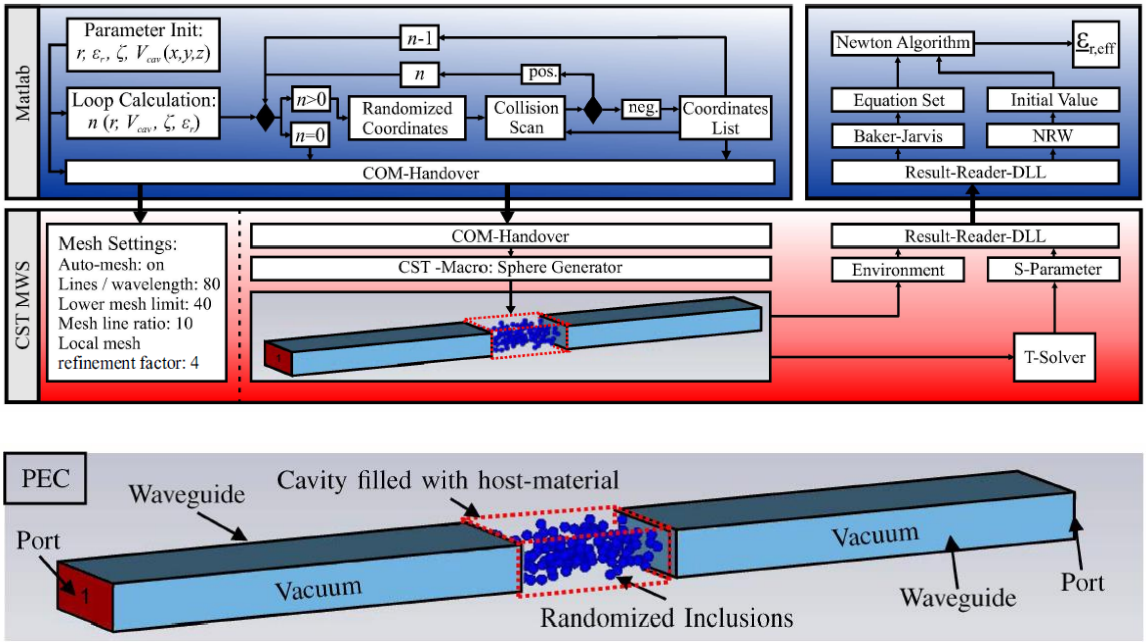

Figure 9. Diagram of the generation, simulation and calculation process © 2015 IEEE [45].

The robust approach to retrieve the effective permittivity and permeability has been programmed into CST MWS as a template based on Ref. [47]. Although this approach was mainly developed for a metamaterial slab, it is directly applicable to a homogeneous slab as the boundaries of the slab and *S*-parameters are well determined [47]. As mentioned above, the EMTs suggest that once the size of the inhomogeneities is much smaller than the wavelength of the electromagnetic wave, a heterogeneous mixture appears homogeneous to the wave [42]. Thus, the robust approach [47] is adequate for calculating the effective properties of mixtures.

3. MANUFACTURING AND MEASUREMENT

The dielectric properties measurements for BST and/or NZF composites in the linear regime allow us to benchmark the models in CST MWS to assess various EMTs for determining the dielectric properties of various composites as the preliminary applications. This chapter briefly summarizes the manufacturing procedures, assessment on the homogeneity of a composite specimen, and dielectric measurement for the composites will be briefly discussed. More details will be provided in the dissertation of one of my colleagues.

3.1. Manufacturing of Composites

The barium-strontium titanate ($Ba_{2/3}Sr_{1/3}TiO_3$, BST) nano-sized powders (TPL, HBS-8000) with an average size of 800 nm and NiZn ferrite (NZF, no composition information) powders (Power Processing & Tech. (PPT), LLC, FP350) with an average size of 17 μm were used. Both powders yielded approximately spherical particles.

3.1.1. Manufacturing procedures

We manufactured composites comprised of BST and/or NZF powders in silicone-based host PDMS. We considered the volume fractions listed in Table 2.

Table 2. Powders volume fractions in composites for manufacturing.

Single inclusion		Mixture	
NZF	BST	NZF	BST
5	5	5	5
10	10	5	10
15	15	10	5
20	20	10	10
25	25	10	15
\	\	15	10

The coaxial mold for making coaxial composites was designed and prepared in advance. The mixture containing powders and PDMS was first stirred by hand and mixed in a mixer (Thinky Mixer AR-100) for a homogenous distribution of inclusions. The bath sonicators (Crest Ultrasonics CP200HT) were used to disperse the nanoparticles and clean the mold with detergent powder (Alconox 1104-1 Powdered Precision Cleaner). The mixture was then placed in a vacuum chamber (Medline Scientific Jeio Tech 665L Vacuum Oven (OV-12)) for 30 minutes at 0.1 MPa for degassing; meanwhile, a mold release spray was used on the mold applying three coats. The degassed mixture was injected into the mold from the bottom to the top while raising the tubing out to prevent introducing voids into the mixture. The mold containing the mixture was next placed in the vacuum chamber again for further degassing. Finally, the mold was cured using the oven (Blue M LO-136E) at 100°C for 2 hours. After the mold and mixture cooled down and were separated, the composite manufacturing was completed.

We made three or four duplicates of each volume fraction to obtain statistical distribution of dielectric properties for each composite with varying volume fractions. The measurements will be presented with simulation results in Chapter 5.

3.1.2. Assessment of composite homogeneity

Composite homogeneity is vital for applying EMTs and CST MWS to predict the dielectric properties and for future application of these dielectric composites particularly at higher volume fractions. The composite samples were assessed for homogeneity using a 3D X-ray Microscope (Zeiss Xradia 510 Versa). Figure 10 shows scan results for an exploratory analysis with a resolution of 4.9275 μm for a combined 15% BST and 10% NZF composite.

The scan clearly shows the distribution of the NZF inclusions, but it could not discern the BST particles from the host PDMS. Future studies will perform additional scans with a resolution of at least 800 nm to distinguish the BST inclusions. The current scan shows a homogeneous distribution of the NZF inclusions except for a few aggregations of the inclusions. The largest aggregations have sizes less than 1 mm. Based on the quasi-static limit, this size is sufficiently small to assume homogeneous distribution of the inclusions.

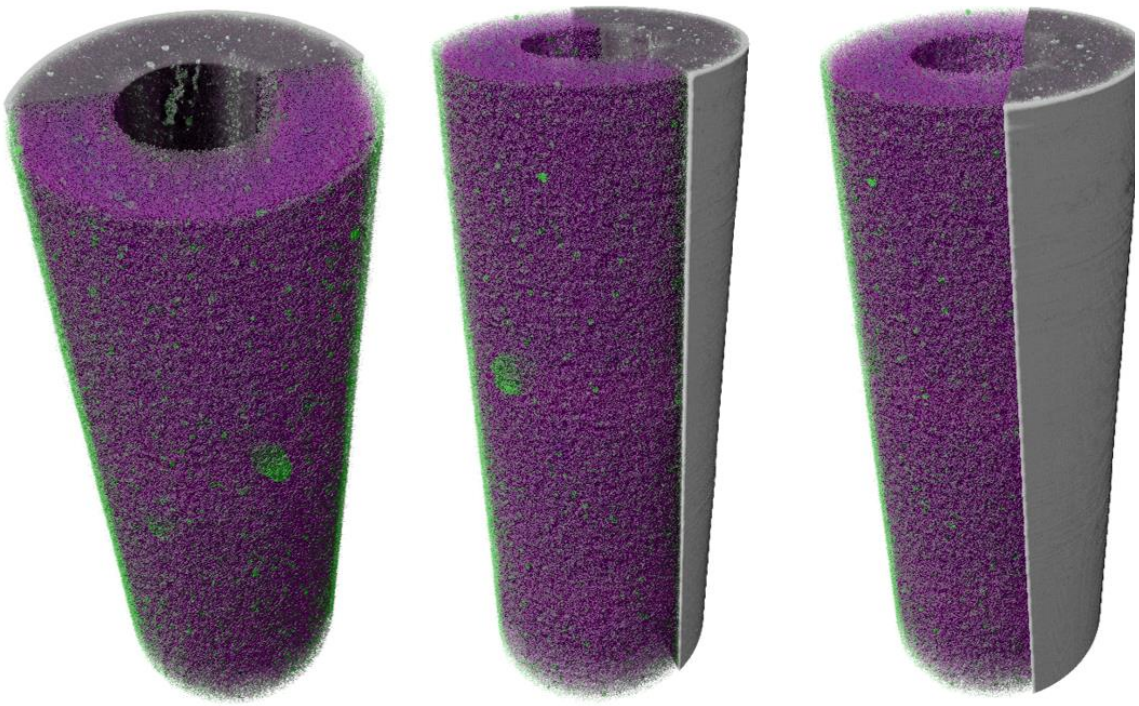

Figure 10. 3D views of interior and exterior of a 15% BST 10% NZF composite. Resolution: 4.9275 μm; Bin:1; Exposure: 9 s.

3.2. Dielectric Measurements in Linear Region

The network analyzer (Keysight FieldFox N9913A) was used to measure the dielectric properties of all the manufactured composites. Figure 11 shows the measurement setup. An anti-static mat and an anti-static wrist strap were applied during the measurement, while gloves were equipped to prevent oils from contaminating surfaces. Calibrations were made before composite measurements using the airline (Keysight 85055A Type-N 50 Ω) to eliminate systematic errors. The dielectric composites were equipped with the outer conductor and inner conductor to form a coaxial transmission line connected with the network analyzer.

Each composite samples is approximately 50 mm long, which exceeds $\lambda_{max}/4$, with λ_{max} evaluated from the lowest $\varepsilon\mu$ at 1 GHz from measurements, with an outer diameter of 7 mm and an inner diameter of 3 mm. The frequency range was set from 1-4 GHz based on the general HPM frequency range of our interests [3], [5].

The power was set to be -15 dBm (voltage: 40 mV). Experiments show that with no bias field (linear region), the relative permittivity measurements of the $Ba_{2/3}Sr_{1/3}TiO_3$ thin film gives almost the same values at 500 MHz for the powers of -20 dBm and 5 dBm [82]. Thus, we assumed the composite measurements at -15 dBm are still in the linear region. Future measurements will specifically examine the nonlinearity of the bulk dielectric properties of the BST ceramic.

Figure 11. The setup of dielectric measurement of composites.

4. SIMULATION METHODS

4.1. Dielectric Properties of NZF and BST

This section introduces the determination of the dielectric properties of two different types of inclusions used in the models due to the situation that the manufactures are not able to provide all the dielectric properties for both materials at 1~4 GHz and we have not measured these dielectric properties yet.

Although several studies report the dielectric properties of these two materials [82]–[87], they might not be applicable to our specific study since the dielectric properties of BST and NZF vary with composition, manufacturing procedures, and measuring conditions and exhibit significant dispersions [82]–[90]. For example, the relative permittivity of $Ba_{2/3}Sr_{1/3}TiO_3$ thin film measured at 12.5 GHz drastically varies with the oxygen pressure during deposition [87]. Thus, we must take caution in using the values from those measurements in our models for assessing our measurements and the EMTs.

Table 3 shows the known and unknown dielectric properties. Some of them were suggested by the manufacturers. The NZF manufacturer did not specify the corresponding frequency for the real permeability, while the BST manufacturer could not provide the frequency for the loss tangent.

Table 3. The dielectric properties of NZF, BST and PDMS. [a] Our measurements at 1 GHz, [b] Database [91], [c] NiZn Ferrite (Power Processing & Tech, LLC, FP350) [92], [d] $Ba_{2/3}Sr_{1/3}TiO_3$ (TPL, HBS-8000) [93].

	ε'	σ (S/m)	μ'	$\tan\delta$	$\tan\delta_m$
PDMS	2.7377 [a]	2.5×10^{-14} [b]	~1[a]	0.0114 [a]	0.0054 [a]
NZF	N/A	10^{-7} [c]	4~6 [c]	N/A	N/A
BST	N/A	10^{-10} [d]	~1[a]	< 0.01[d]	~0 [a]

The temporary approach to obtain the dielectric properties of the NZF and BST in this experiment involves fitting the physical based EMTs to our composite measurements, using data from the literature to determine the most applicable inputs for the models under our current conditions.

Using the conductivities reported in Table 3 for NZF and BST in the EMTs yielded imaginary permittivity and permeability in poor agreement with measurements. Instead, we applied the composite models in CST MWS to tune the input values to fit with measurements based on the order of magnitude suggested in literature for losses, although the chemical composition of our NZF is unknown.

4.1.1. The permeability and permittivity of NZF

We estimated the dielectric properties of NZF by fitting the experimental values with different inputs, applying different classical EMTs and the least-squares method. The minimum of the sum of squared residuals indicates the estimated relative permittivity or permeability for NZF. We estimate the relative permittivity by minimizing the sum of squared residuals *S*, given by

$$S = \sum_{v} (\varepsilon_E - \varepsilon_m)^2 \tag{27}$$

where v represents the volume fractions, ε_E is the calculated value from the classical EMTs using various assumed values, and ε_m is the experimental value at a specific frequency. From NZF composite measurements, the relative permittivity shows almost no frequency dependence, while the permeability shows an increasing frequency dependence when the volume loading goes higher. Considering the relative permittivity of NZF at 1~4 GHz as a constant should be acceptable, thus we estimated the permittivity at 1 GHz and the permeability at 1~4 GHz, as shown in Figure 12.

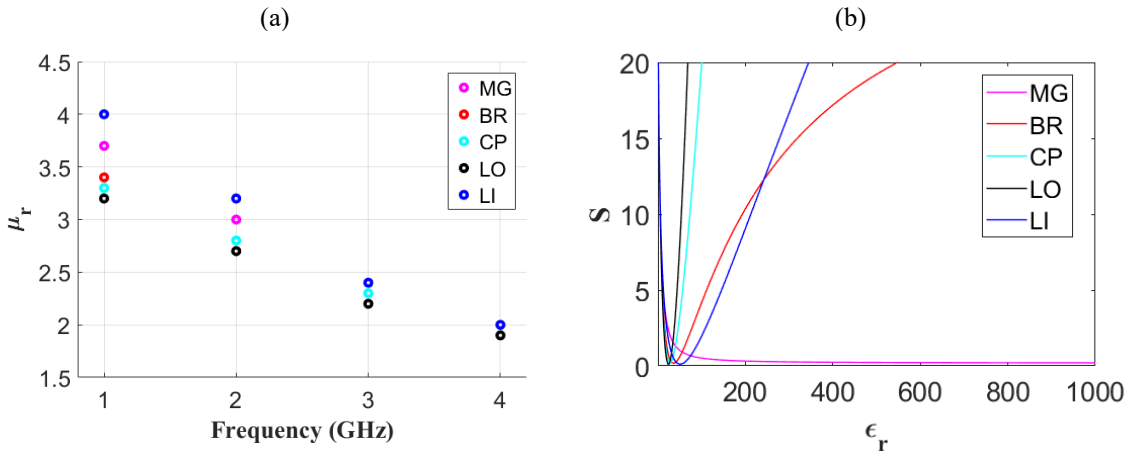

Figure 12. The estimations from the least squares method for (a) the NZF relative permeability at 1~4 GHz, (b) the NZF relative permittivity at 1GHz. The applied EMTs: MG: Maxwell- Garnett, BR: Bruggeman, CP: coherent potential, LO: Looyenga, LI: Lichtenecker.

The various classical EMTs gave relatively similar values for the real permeability of NZF. With increasing frequency, the real permeability decreases, and the estimations get closer, as shown in Figure 12 (a). In addition, among all the applied EMTs, the LI rule gives $\mu_r = 4$ at 1 GHz which is in the typical range of $4 < \mu_r < 6$ provided by the manufacturer. However, estimates for ε_r range from 23 (LO) to 52 (LI). Because we have not found

measurements indicating that ε_r reaches 100 at GHz frequencies, we do not consider the MG from Figure 12 (b) as reasonably estimating ε_r for our experiments.

4.1.2. The permittivity of BST

For the permittivity of BST, the use of the assumed inputs from 1 to 1000 the MG rule fails to give a minimum of *S* again, while other classical EMTs give the estimations ranging from 51 (LO) to 162 (LI), as illustrated in Figure 13, which are lower than the experimental values from two measurements for a $Ba_{2/3}Sr_{1/3}TiO_3$ thin firm [82], [83].

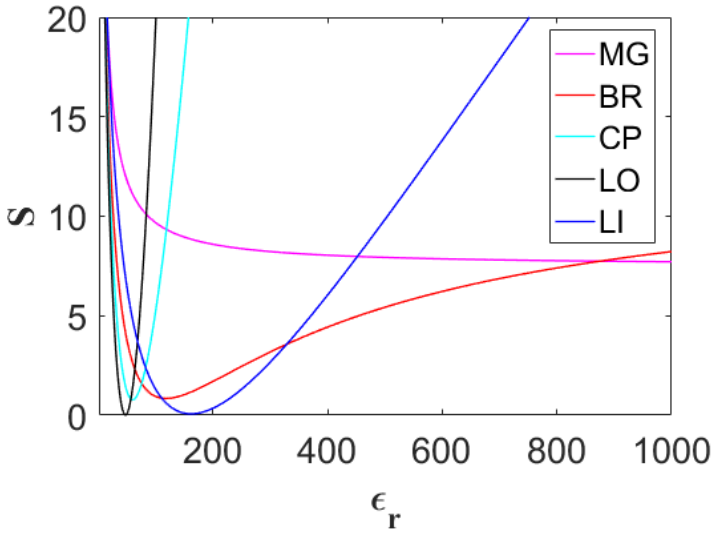

Figure 13. Sum of squared residuals for determining the relative permittivity of a BST inclusion. The estimations from the least squares method for the relative permeability of BST at 1 GHz.

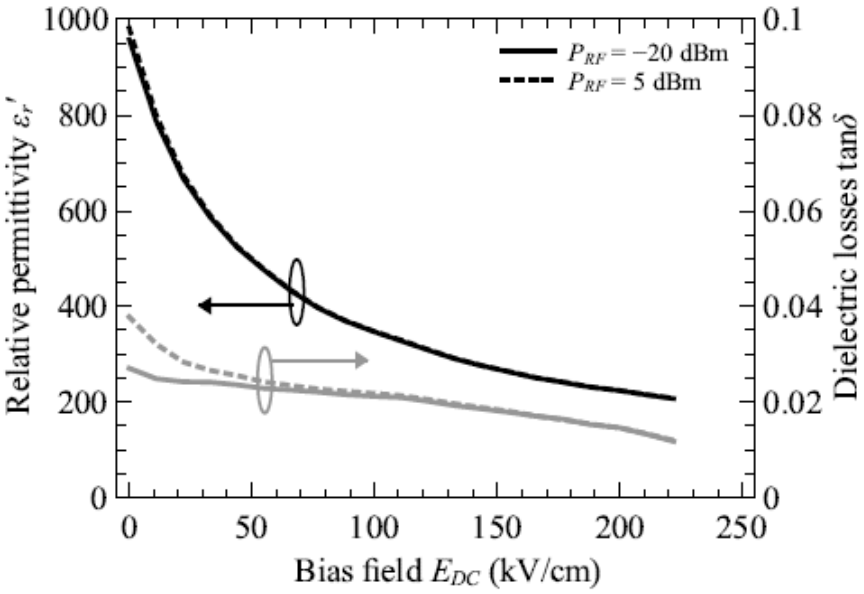

Figure 14. The relative permittivity and dielectric losses varying with bias field for two incident powers at 500 MHz. Reproduced with permission from Appl. Phys. Lett. 110, 212902 (2017). Copyright 2017, American Institute of Physics [82].

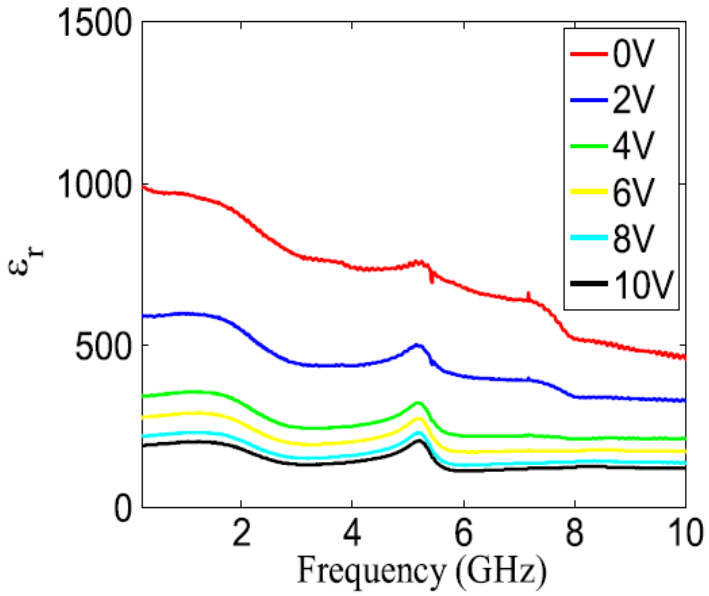

Figure 15. Relative permittivity of BST as a function of frequency and bias voltage © 2016 IEEE [83].

Figures 14 and 15 show that the two measurements give almost the same relative permittivity for BST (≈960) at 500 MHz [82] and 1 GHz [83]. In addition, the two

measurements exhibit similar voltage dependence of the permittivity. Although we assume that there is negligible dispersion from 500 MHz to 1 GHz and that these two measurements use the same BST, it is still difficult to definitely conclude that $\varepsilon' \approx 960$ is applicable for our case. However, this experimental value can be used to provide an order of magnitude estimate for a starting point in CST MWS allowing us to tune the permittivity input of BST to match our measurements for an initial assessment.

4.2. Composite Models in CST Microwave Studio

4.2.1. Composite model design

The dielectric composite models extend the advancements made in recent simulation and theoretical works [45], [47]. The following section presents the simulation procedure for determining the relative effective permittivity and permeability of the composites. The simulation procedure consists of three steps: (1) generating random spherical inclusions, (2) designing the composites model and selecting the simulation settings, and (3) extracting the effective properties.

This procedure is similar to that reported in Ref. [45], and summarized in Figure 9. We used MATLAB to generate random coordinates for various volume loadings of spherical inclusions within a rectangular space with volume V. The total volume of the inclusions was simply defined as $V_{in} = 4n\pi r^3/3$, where r is the radius of an individual spherical inclusion and n is the number of inclusions necessary to achieve a volume loading $f = V_{in}/V$. The actual volume fractions of the generated inclusions are not exactly equal to the

designated ones because of the discrete volume of a single inclusion. Although these errors may be mitigated by reducing the inclusion radius, the percentage errors of the simulated volume fractions are almost negligible, as shown in Figure 16.

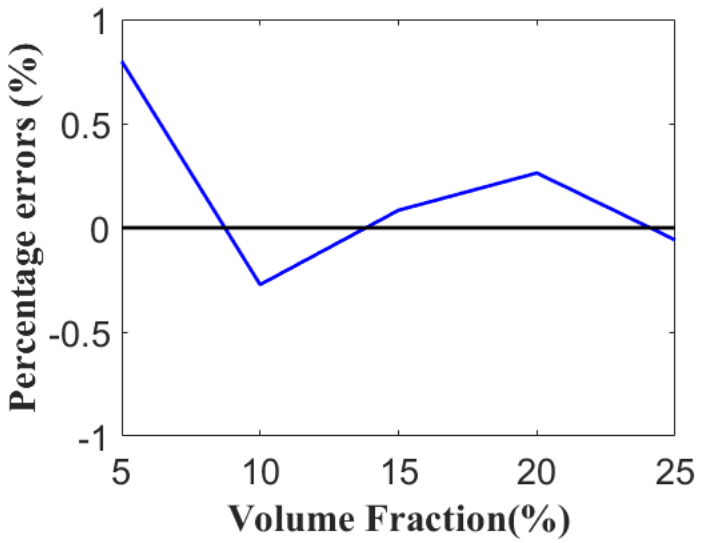

Figure 16. Relative percentage errors of the simulated inclusion volume as a function of volume fraction for 0.2 mm radius spherical inclusions.

We considered hard spheres for the inclusions by setting the distance of each arbitrary coordinates greater than or equal to $2r$ to ensure the spherical inclusions did not overlap. In addition, the models assume that any air bubbles or voids produced during manufacturing are negligible, so we only have to consider the spherical inclusions.

In the second part, a rectangular waveguide was created with volume V to represent the host material PDMS. We then saved the generated coordinates of the randomly distributed inclusions as text files and transferred them to CST MWS via a self-made CST VBA Marcos to generate spheres inserted in the host material PDMS. The front and back (z-direction) use the open boundary condition, whereas the left and right (x-direction) apply

the perfect magnetic conductor (PMC) boundary condition and the top and bottom (y-direction) use the perfect electric conductor (PEC) boundary condition [94], as shown in Figure 17.

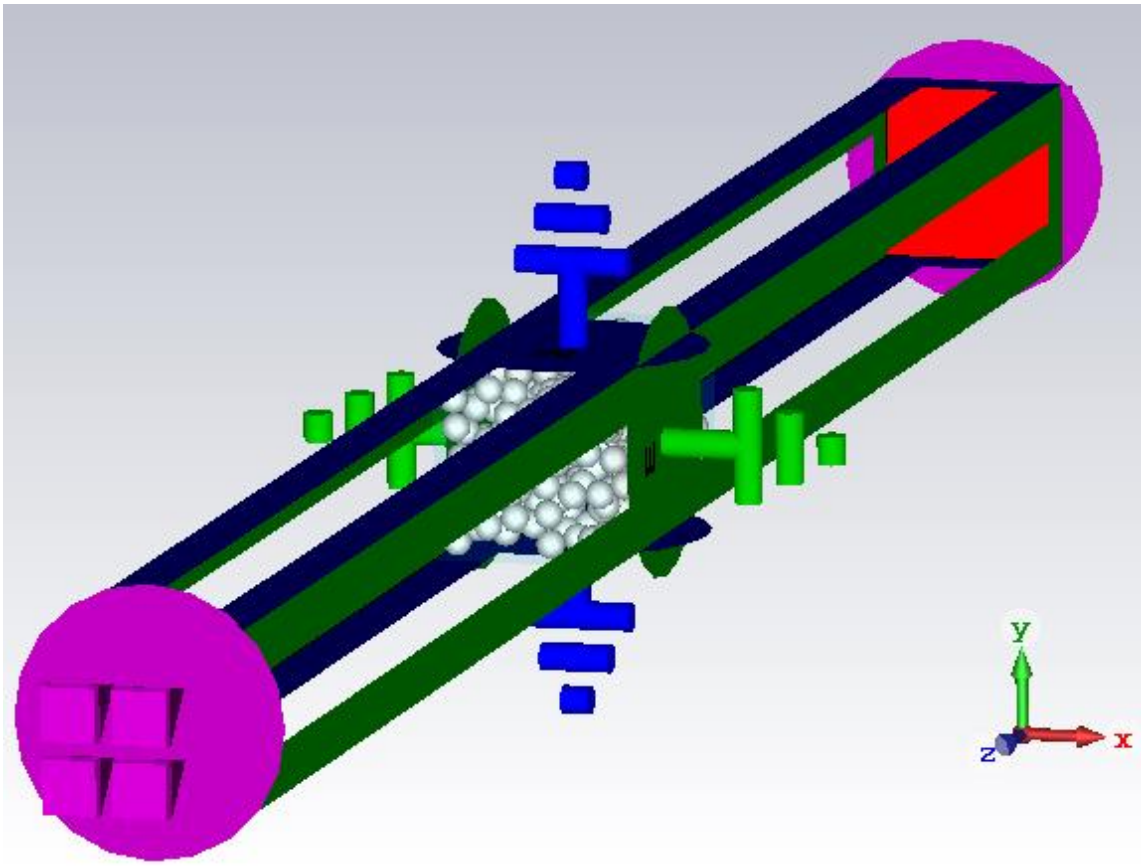

Figure 17. An illustration of the model in CST MWS. Background material type: normal; Boundary conditions: X_{min}: $E_t = 0$, X_{max}: $E_t = 0$, Y_{min}: $H_t = 0$, Y_{max}: $H_t = 0$, Z_{min}: open, Z_{max}: open.

The time-domain solver was used to solve for the S-parameters. The accuracy of the solver is -30 dB, and mesh settings were introduced in the mesh size section. After the solver finished, we obtained the S-parameters and extracted the permittivity and permeability using a template for post-processing based on the numerical method in Ref. [47].

4.2.2. Inclusion size based on the quasi-static limit

For validating the quasi-static limit of the EMTs, the radius *r* should be set sufficiently small based on the quantitative criterion in (24). The wavelength in the mixture λ can be written as

$$\lambda = \frac{c}{f\sqrt{\varepsilon_{eff}\mu_{eff}}} \tag{28}$$

where ε_{rc} and μ_{rc} are the relative effective permittivity and permeability of the composite, and f is the frequency. Using the maximum product of relative permittivity and permeability based on one of the composite measurements ($\varepsilon_{eff}\mu_{eff}$ = (6.1297)×(1.4497) = 8.886, for a 25% NZF composite) at the highest frequency (4 GHz) in (28) to calculate the shortest wavelength (25.159 mm) among all composites and frequencies studied here. This means that the maximum inclusion size to make the quasi-static limit valid is approximately 4 mm.

However, to obtain a homogenous distribution of inclusions, applying relatively large radius of inclusions, such as 1 mm, requires relatively large dimensions of the bulk composite (25 mm, 25 mm, 50 mm) in CST. This will induce discontinuities of effective dielectric properties which may be induced by resonances [47]. Although the dielectric properties at some frequencies rather than a resonance band are equal to that from the same model but using a smaller inclusion size and smaller bulk dimensions inducing no discontinuities at 1~4 GHz, we decided to use a smaller radius of inclusions considering the frequency dependences of some dielectric properties.

We tested two different inclusion radii (r = 0.1 mm and 0.2 mm) with the same bulk dimensions (2.5mm, 2.5 mm, 5 mm) and the same mesh settings (the minimum mesh size: 0.005 mm) in CST composite models with the input values: real permittivity ε_i = 1000 and real permeability μ_i = 4 for inclusions and ε_h = 2.73773 and μ_h = 4 for host. For both inclusion sizes, the products $\varepsilon_{eff}\mu_{eff}$ are approximately equal to 10.04 at 4 GHz.

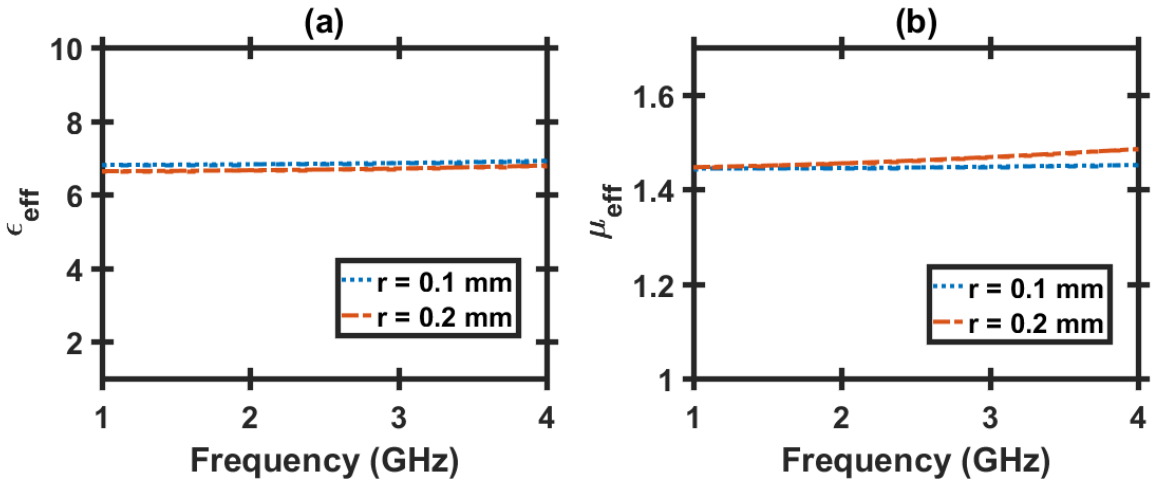

Figure 18. (a) Effective permittivity, and (b) effective permeability of composites with real permittivity ε_i = 1000 and real permeability μ_i = 4 for inclusions and ε_h = 2.73773 and μ_h = 1 for host.

It was noticed that there are small frequency dependences in ε_{eff} and μ_{eff}, as shown in Figure 18, and with r = 0.2 mm the data shows relatively larger variation from 1 to 4 GHz due to greater heterogeneity and inclusion size. We speculated that this variation could be induced by the numerical method for extracting ε_{eff} and μ_{eff} and due to the resonance band at frequencies higher than 4 GHz [47], also it could be due to the size (r = 0.2 mm) is not sufficiently small at higher frequencies for this composite modeling. For r = 0.1 mm, the frequency dependences are mitigated and negligible.

Additionally, the variation between r = 0.2 mm and 0.1 mm for ε_{eff} should be induced by the mesh settings, because using the same minimum mesh size of 0.005 mm will result in relatively greater error (higher ε_{eff}) for r = 0.1 mm than for r = 0.2 mm, as detailed in the next section.

The first variation (frequency dependence) has similar values with the second one induced by mesh size, and both are approximately equal to or less than 2%. We set r = 0.2 mm for all composite models for better simulation efficiency. Based on our measurements, most composites have the product $\varepsilon_{eff}\mu_{eff} \leq$ 8.886. Thus, we considered the first variation is acceptable and r = 0.2 mm is small enough for the quasi-static limit for current assessments.

4.2.3. Mesh sizes

Figure 19 shows a mesh view for a composite model in CST MWS. For the mesh settings in the time domain solver, the hexahedral mesh cells outside the rectangular composite bulk can be relatively large. In the rectangular composite bulk, the mesh size for the inclusions should be set sufficiently small to obtain good accuracy due to the difference of the dielectric properties between the host and the inclusions. However, it has been failed to set different local mesh properties for the host material PDMS and the BST or NZF inclusions to make finer mesh cells for the inclusions or around them. The unified mesh size in the rectangular composite bulk considerably increases the simulation time if a fine mesh cell size is set for the inclusions.

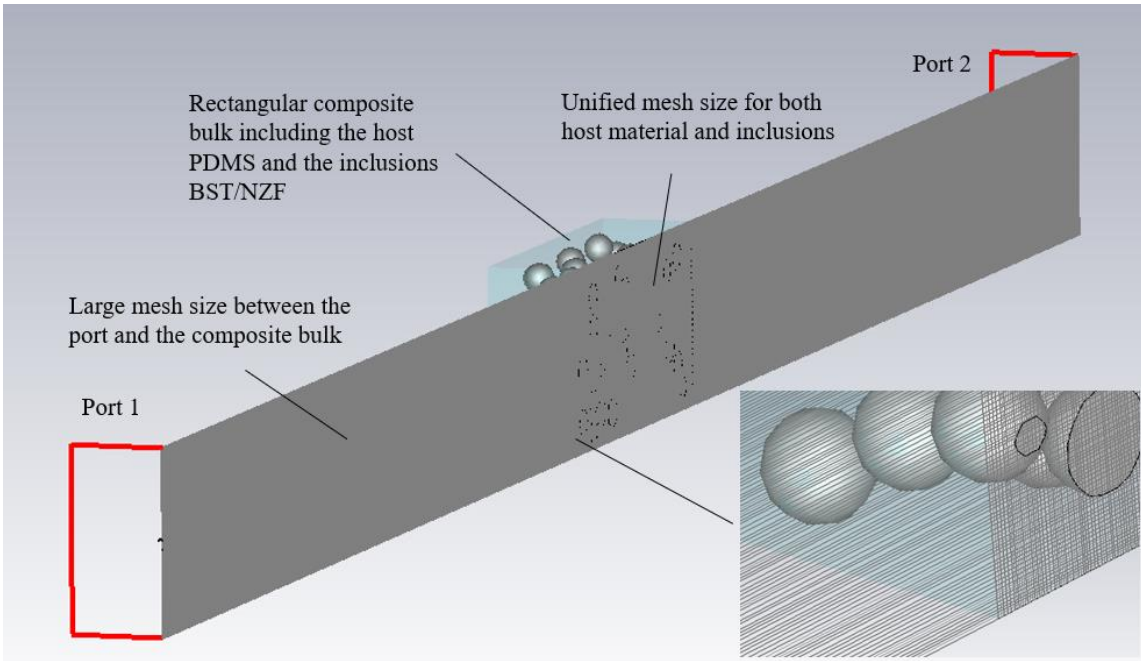

Figure 19. A cut plane of composite geometry demonstrating the meshing for a CST MWS simulation.

Moreover, based on our simulation results, if a mesh cell contains a portion of an inclusion with higher dielectric properties than host, CST MWS will define the mesh cell as inclusion, inducing redundant volume of inclusions and overpredicting effective dielectric properties. Thus, a model with ultra-high values of dielectric properties of the inclusions, such as the real permittivity of BST, require even finer mesh cells to obtain accurate results, making the model very computationally expensive. The relatively large number of inclusion conditions required for screening here necessitated defining the simulation mesh sizes to achieve acceptable errors with a reasonable simulation time rather than strictly optimizing simulation accuracy.

We used adaptive mesh refinement to determine the mesh size/number ranges with acceptable accuracy and simulation time for 25% BST (with the highest input $\varepsilon' = 960$)

and 25% NZF (with the highest input $\varepsilon' = 52$) in the composite models. The mesh settings were then manually adjusted based on the ranges for obtaining converged results of the effective permittivity.

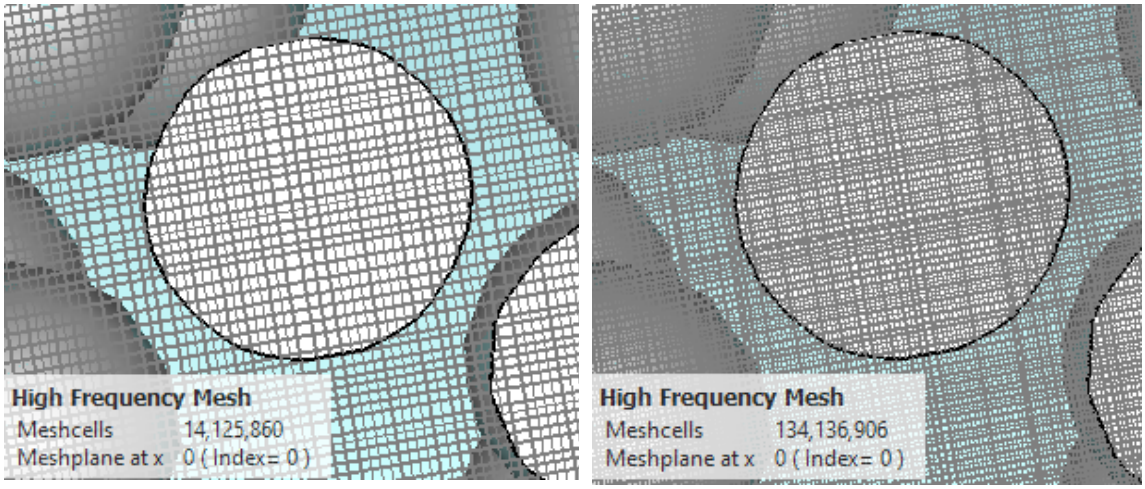

Figure 20. Cut planes demonstrating the meshing for mesh sizes of 0.01 mm (left) and 0.005 mm (right).

We found that when the minimum mesh size for BST and NZF composite models were set to 0.01 mm and 0.02 mm, respectively, further reducing the mesh sizes by half to 0.005 mm and 0.01mm, respectively would change the results by approximately 3% for a 25% composite model, while requiring a significant amount of additional simulation time. For example, models with 0.005 mm and 0.01 mm mesh sizes require approximately 72 hours and 15 hours to finish, respectively. For composite models with lower volume loadings, the variations are less than 3%, since the errors are basically induced by the relatively large mesh cells on the inclusion surfaces.

Using 0.005 mm for the mesh size yields the same order of magnitude of mesh cells (~10^8) as in Ref. [45], as shown in Figure 20, but we were not able to run the solver with this mesh

size or accuracy. We successfully ran simulations with mesh settings of 0.01 mm and 0.02 mm for BST and NZF, respectively, for the current assessments. In fact, considering the standard deviations of the composite measurements and potential inaccuracy of the inputs of the dielectric properties, the errors induced by the mentioned mesh settings should be minimal and acceptable for the current calculations.

5. RESULTS AND DISCUSSION

The NZF, BST and combined BST and NZF composite models in CST MWS were performed for various volume fractions using the dielectric properties of NZF and BST from estimates based on fitting our composite measurements to the classical EMTs and the tuned values based on literature measurements for the bulk materials. Then the simulation results in CST MWS will be presented compared with the composite measurements and the classical EMTs calculations. However, the classical EMTs are limited to the cases without strong dielectric contrast, such as the real permittivity and permeability of NZF composites.

5.1. NZF Composites

By testing the various estimates using the classical EMTs in CST MWS models, we found that the CST simulations agreed best with the measurements when using the estimated real permittivity and permeability of NZF from the Lichtenecker (LI) rule. Since classical EMTs failed to estimate the imaginary permittivity and permeability of NZF, we used tuned values of the loss tangent and magnetic loss tangent to assess the losses of the NZF composites.

5.1.1. Real permittivity and permeability of NZF composites

The inputs of PDMS for the real permittivity and permeability were set as constants based on our measurements, as shown in Figure 27. For the real permittivity of NZF composites,

we considered a constant real permittivity of NZF for 1 to 4 GHz as acceptable, since the measurements show negligible dispersion in this frequency range.

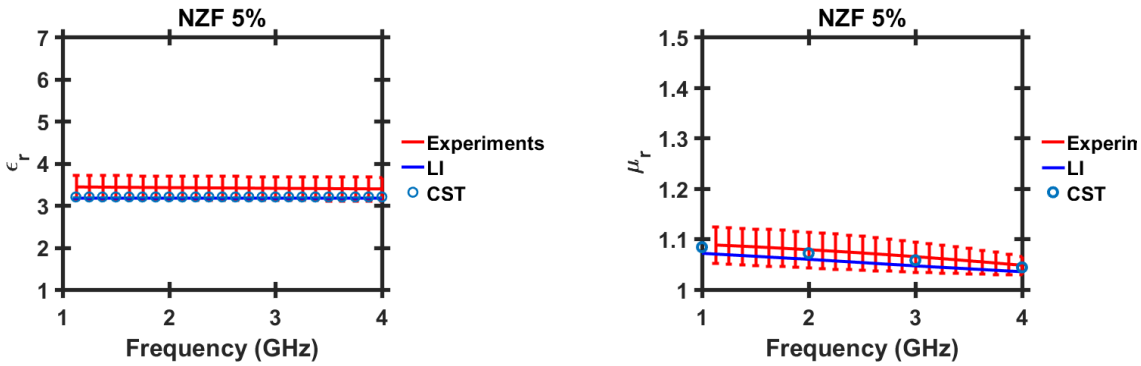

Figure 21. Effective real permittivity and permeability of 5% NZF composite from the measurements (with error bars), the LI (Lichtenecker) rule and CST MWS simulation (CST).

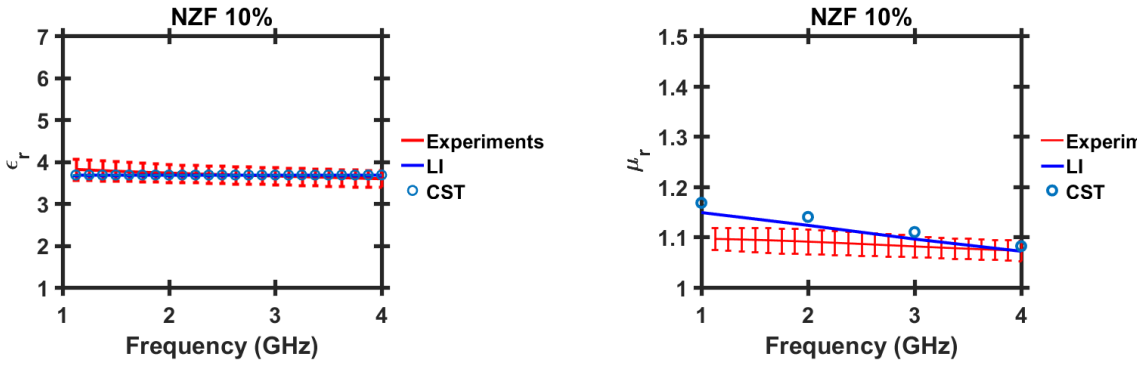

Figure 22. Effective real permittivity and permeability of 10% NZF composite from the measurements (with error bars), the LI (Lichtenecker) rule and CST MWS simulation (CST).

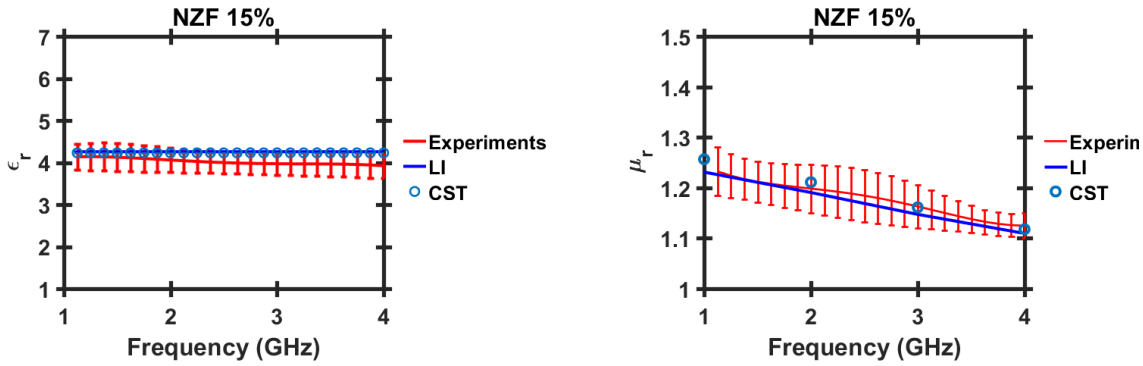

Figure 23. Effective real permittivity and permeability of 15% NZF composite from the measurements (with error bars), the LI (Lichtenecker) rule and CST MWS simulation (CST).

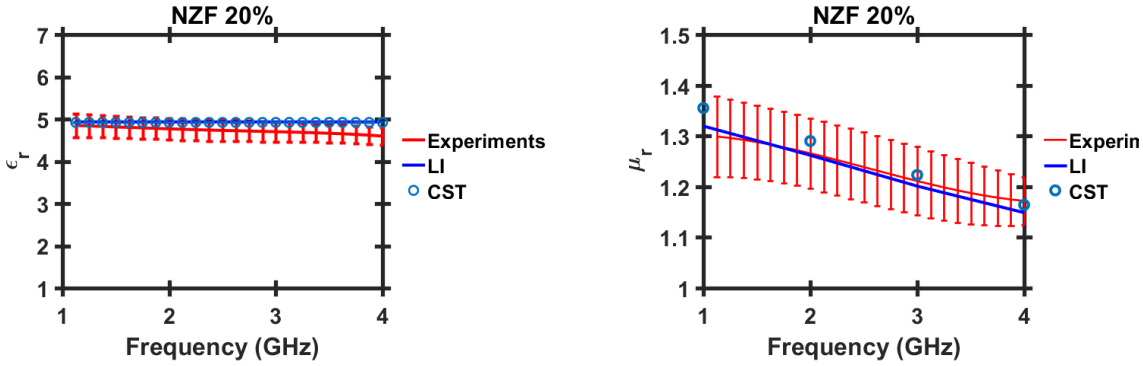

Figure 24. Effective real permittivity and permeability of 20% NZF composite from the measurements (with error bars), the LI (Lichtenecker) rule and CST MWS simulation (CST).

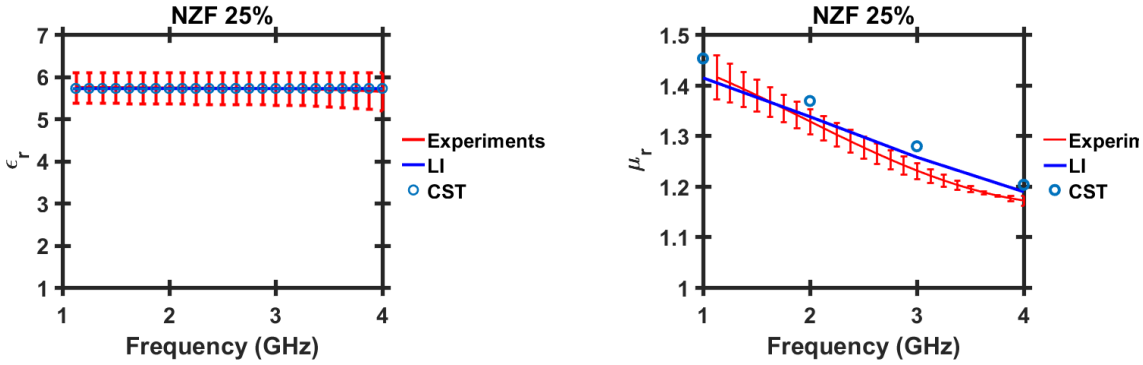

Figure 25. Effective real permittivity and permeability of 25% NZF composite from the measurements (with error bars), the LI (Lichtenecker) rule and CST MWS simulation (CST).

The real permeability of NZF shows greater frequency dependence for higher volume loading, suggesting a frequency-dependent dielectric spectrum of the permeability of NZF. By using the frequency-dependent fitting values of the real permeability of NZF at 1 ~ 4 GHz, the effective real permeability of the composites in CST MWS models agree well with the measurements and LI rule, and the simulation describes the dispersions for all volume fractions except for 10% NZF composites, as shown in Figure 21-25. However, Figure 26 shows that the measured permeability for the 10% NZF composites is unexpectedly low compared to the 5% and 15% loadings (and almost the same as the 5% loading). Future studies should reconsider these volume loadings to assess for potential measurement, analysis, or material issues.

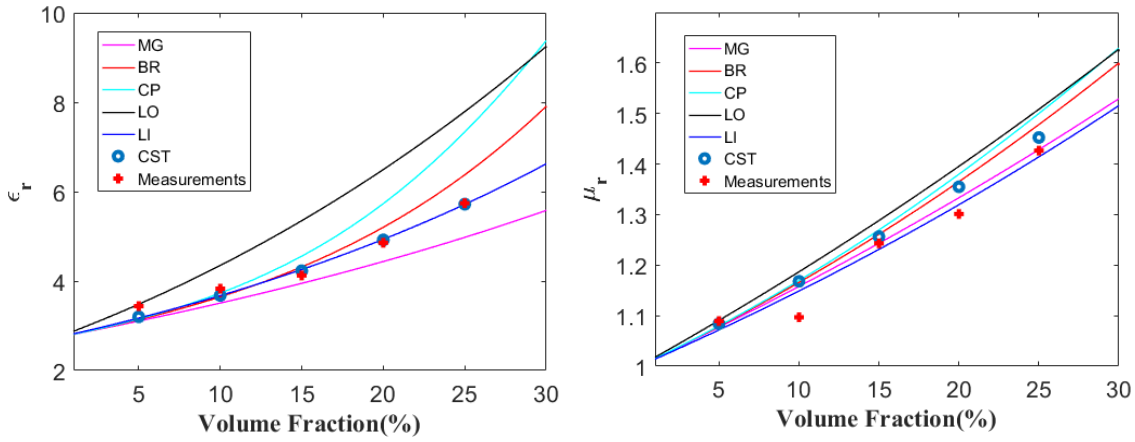

Figure 26. Results comparison of the effective real permittivity (left) and permeability (right) of NZF composites as a function of inclusion volume fraction at 1 GHz. The applied effective medium theories (EMTs): MG: Maxwell- Garnett, BR: Bruggeman, CP: coherent potential, LO: Looyenga, LI: Lichtenecker.

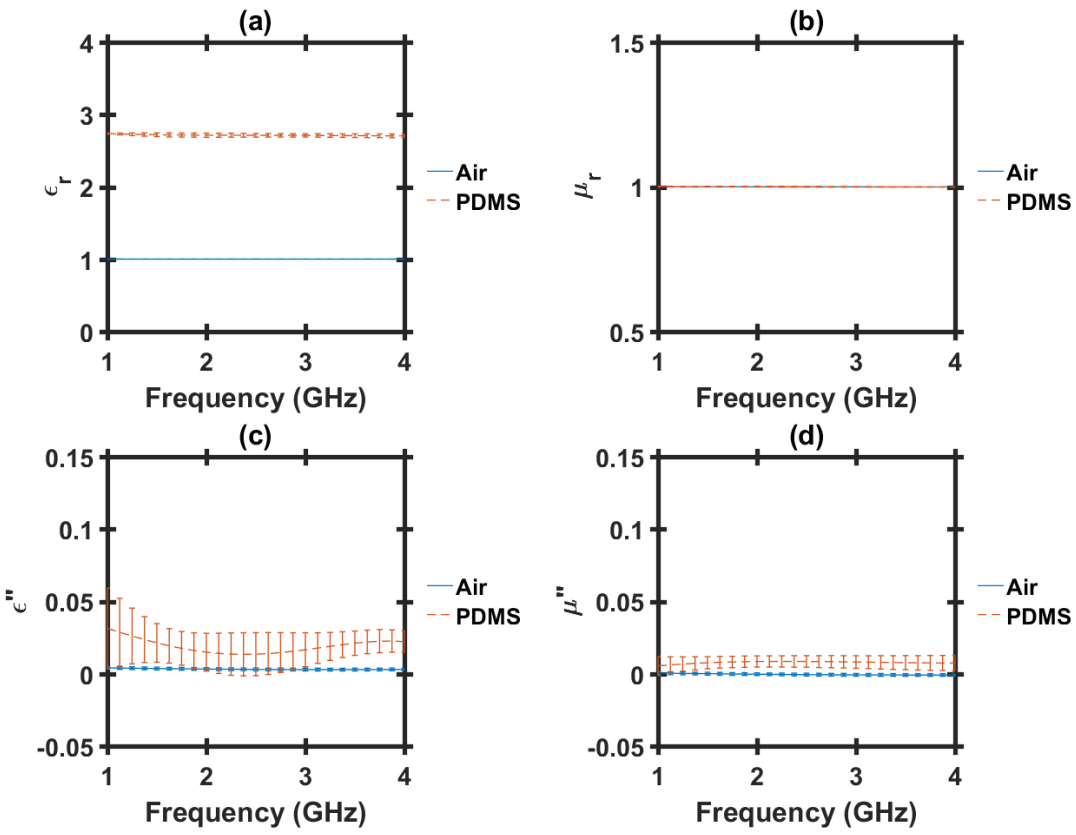

Figure 27. Measurements of the dielectric properties of PDMS and air.

5.1.2. Dielectric and magnetic losses of NZF composites

Since the fitting method using the classical EMTs does not yield estimates for imaginary permittivity and permeability of NZF, we considered using the data from the measurements in Ref. [84] and [86] as starting points for tuning the inputs in CST MWS. It should be noted that the chemical composition of our NZF powder is unknown and might not be the same as used in these other studies.

We incorporated the dielectric losses of PDMS based on our measurements reported in Figure 27 into our models. Applying the NZF measurement data ($\tan\delta$ = 0.006 and

$\tan\delta_m$= 0.065 at 1 GHz [84]) underestimated the effective imaginary permittivity and permeability. After we tuned the inputs to match the composite measurements, we found that using $\tan\delta$ = 0.06 and $\tan\delta_m$= 0.5 for NZF at 1 GHz gave the best fit with the composite measurements in order of magnitude, as shown in Figure 28.

Using $\tan\delta$ = 0.06 can assess the contribution from the conductivity for the dielectric loss of NZF. The relative imaginary permittivity ε'' can be written as

$$\varepsilon'' = \varepsilon_d'' + \frac{\sigma_s}{\varepsilon_0\omega} \tag{29}$$

where ε_d'' is the loss from the dipole moment rotation (noted that the notations here is different from Ch.2, ε' and ε'' represent the relative real and imaginary permittivity, respectively, for simplicity), σ_s is the conductivity (with an assumption of a static conductivity for NZF, and $\sigma_s =$ 10^{-7} S/m), $\sigma_s/(\varepsilon_0\omega)$ stands for the loss induced by conduction. The loss tangent can be written as

$$\tan\delta = \frac{\omega\varepsilon_d''\varepsilon_0 + \sigma_s}{\omega\varepsilon'\varepsilon_0} = \frac{\varepsilon''}{\varepsilon'} \tag{30}$$

where ε' is the relative real permittivity (with $\varepsilon' =$ 52 for NZF). Applying a frequency at 1 GHz, then ε'' and $\sigma_s/(\varepsilon_0\omega)$ in (29) can be calculated as 3.12 and 1.7976×10^{-6}, respectively, suggesting a negligible loss contribution from the conductivity. Thus, the relative imaginary permittivity ε'' is approximately equal to ε_d''.

Since the dipole moment rotation ε_d'' dominates $\sigma_s/(\varepsilon_0\omega)$, we cannot determine a frequency-dependent ε'' or $\tan\delta$ by assuming the static σ_s and using appropriate

analytical equations. We considered tuning the frequency-dependent loss tangent at other frequencies, but the models become computationally expensive when they include the loss calculations. Currently, we can only estimate the order of magnitude of the losses at 1 GHz for various volume loadings but not frequency-dependent losses ranging from 1 to 4 GHz.

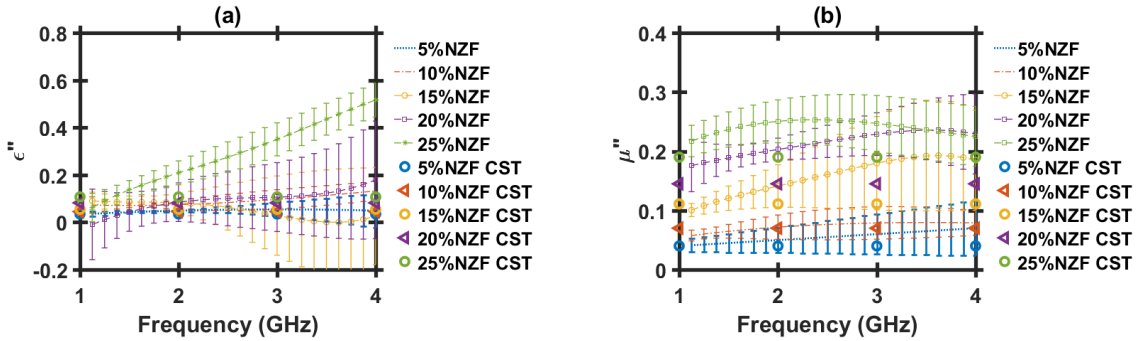

Figure 28. Results comparisons of (a) Effective imaginary permittivity and (b) effective imaginary permeability of NZF with the tuned values of NZF: $\tan\delta = 0.06$ and $\tan\delta_m = 0.5$. The lines with error bars are from measurements.

If the tuned values $\tan\delta = 0.06$ and $\tan\delta_m = 0.5$ are correct or close to the actual values, the imaginary permittivity and permeability can be calculated as $\varepsilon''_{NZF} = 3.12$ and $\mu''_{BNZF} = 2$. The calculated imaginary permittivity and permeability are much greater than that of PDMS, yielding strong electrical contrasts of the imaginary parts between the host and the inclusions. This explains why the classical EMTs do not accurately account for the imaginary permittivity and permeability of NZF.

5.2. BST Composites

The EMTs fitting method failed to estimate the real permittivity and the imaginary permittivity and permeability of BST. Thus, we considered using the literature values from measurements of BST with the same chemical composition ($Ba_{2/3}Sr_{1/3}TiO_3$) as ours. Two

measurements reported $\varepsilon'_{BST} \approx 960$ at 500 MHz [82] and 1 GHz [83]. However, entering this value into the CST as an input in BST composite models gave relatively lower results compared with measurements, as shown in Figure 29 (a).

We varied ε'_{BST} up to 2500 in 25% BST composite model but remaining the same mesh sizes as 0.01 mm due to simulation time constraint, and the results were still lower than the measurements, as shown in Table 4. Note that increasing the inclusion permittivity in CST MWS requires using a finer mesh size to prevent errors that will overpredict ε_{eff}. Considering the increase of ε_{eff} introduced by increasing ε'_{BST} and the errors induced by the relatively large mesh size for higher permittivity inputs, ε_{eff} should increase significantly in the composite models; however, it did not. This indicates that the real permittivity of BST could be even higher than the values used in Table 4.

Table 4. Effective real permittivity of 25% BST composite models with various tuned inputs of the real permittivity of BST compared with measurements. The mesh size of the inclusions remains 0.01 mm.

ε'_{BST}	960	1500	2000	2500	Measurements
ε_{eff}	6.87	7.05	7.16	7.23	7.45

However, we cannot currently run the simulations with higher values of ε'_{BST} and finer mesh sizes to obtain the best fit with our composite measurements. We will soon receive the necessary equipment to measure the real permittivity of our BST to determine the precise inclusion parameters to use in the composite theory and simulation. This will further elucidate whether the challenges we have encountered arose due to uncertainty in inclusion parameters or other mechanisms we have yet to identify.

For the current assessment, we used the real permittivity and loss tangent of BST from Refs. [82] and [83] (ε'_{BST} = 960 at 1 GHz, $\tan\delta$ = 0.021 at 500 MHz) and the measurements of PDMS from Figure 27 in the BST composite models. Figure 29 shows the results from this simulation. The imaginary permittivity from simulation agrees well with measurement at 1 GHz in terms of orders of magnitude, consistently underpredicting experimental results for the real permittivity. This may suggest some common factor (perhaps an underestimation of the inclusion permittivity) requires adjustment; however, more data is required concerning the dispersions of the effective ε''_{BST} to further benchmark to theory.

Using $\tan\delta$ = 0.021 and ε'_{BST} = 960, ε''_{BST} = 20.16. Using (29) and (30) to calculate $\sigma_s/(\varepsilon_0\omega)$ and comparing with ε''_{BST} = 20.16 suggests that the loss contribution from the conductivity is negligible (assuminga static conductivity for BST and $\sigma_s = 10^{-10}$ S/m). The comparison between the imaginary permittivity $\varepsilon''_{PDMS} < 0.05$ and ε''_{BST} = 20.16 also explains why the classical EMTs failed to yield estimates.

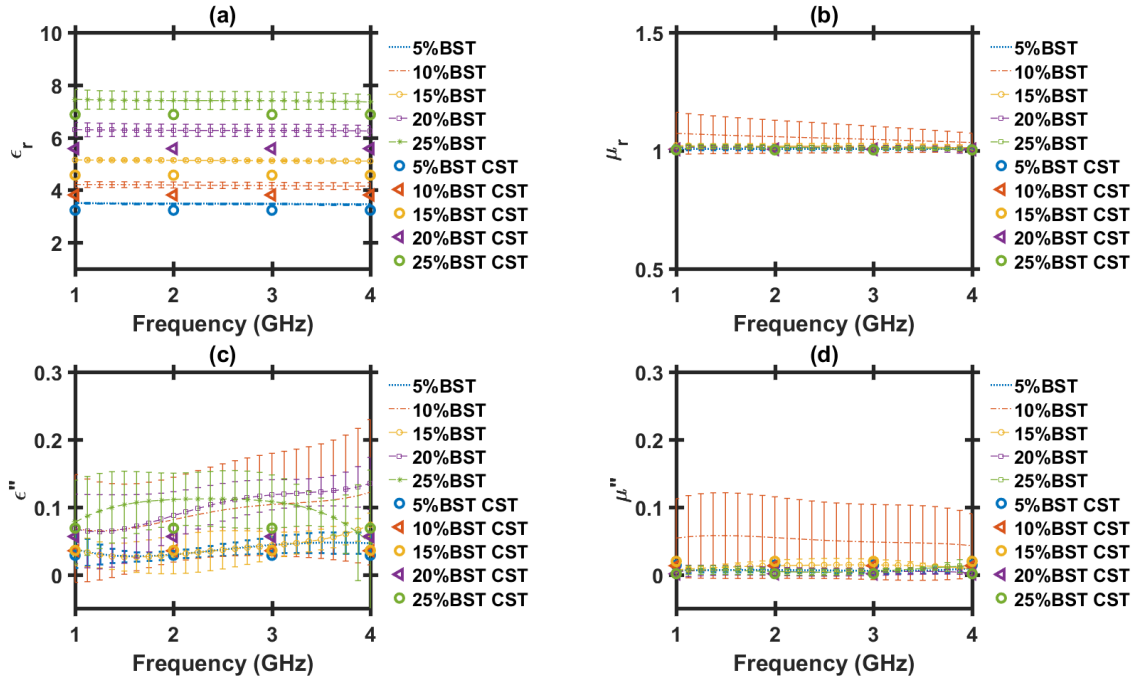

Figure 29. Results comparisons of BST composites (a) the effective real permittivity, (b) the effective real permeability, (c) the effective imaginary permittivity, (d) the effective imaginary permeability. The lines with error bars are from measurements. The inputs in CST MWS for BST: ε'_{BST} = 960, $\tan\delta$ = 0.021 (at 500 MHz), μ'_{BST} = 1, $\tan\delta_m$ = 0.

Figure 30 shows the effective real permittivity varying with volume fractions for BST composites. With the same input ε'_{BST} = 960, CST MWS models gave the closest estimates to measurements. The BR rule agrees well with measurements when the volume fraction is below 20%. Except for the MG rule all other applied classical EMTs generally overestimate the effective permittivity. Compared with the data presented in Figure 26 and 30, the classical EMTs generally fail to give a consistent estimate when the electrical contrast gets stronger.

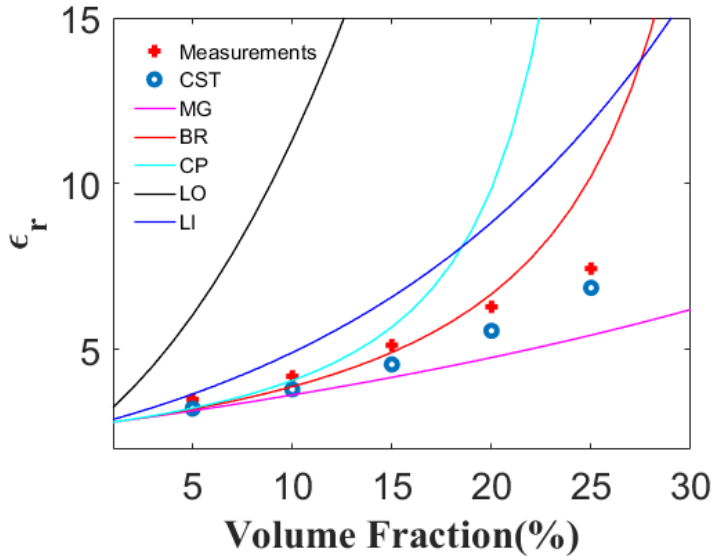

Figure 30. Results comparison of real permittivity of BST composites at 1 GHz varying with volume fractions. All the classical EMTs applied the same input ε'_{BST} = 960.

5.3. Combined BST and NZF Mixing Composites

In combined BST and NZF mixing composite models, we applied the inputs of BST and NZF from the previous determinations of the dielectric properties. Figure 31-34 show the simulation results compared with measurements. The BST & NZF composite models generally underestimate the effective real permittivity, while they agree with measurements for the effective permeability except 10% BST &15% NZF composites at low frequencies. The BST & NZF composite models gave reasonable fit for the effective imaginary permittivity and permeability except for the dispersions at higher frequencies.

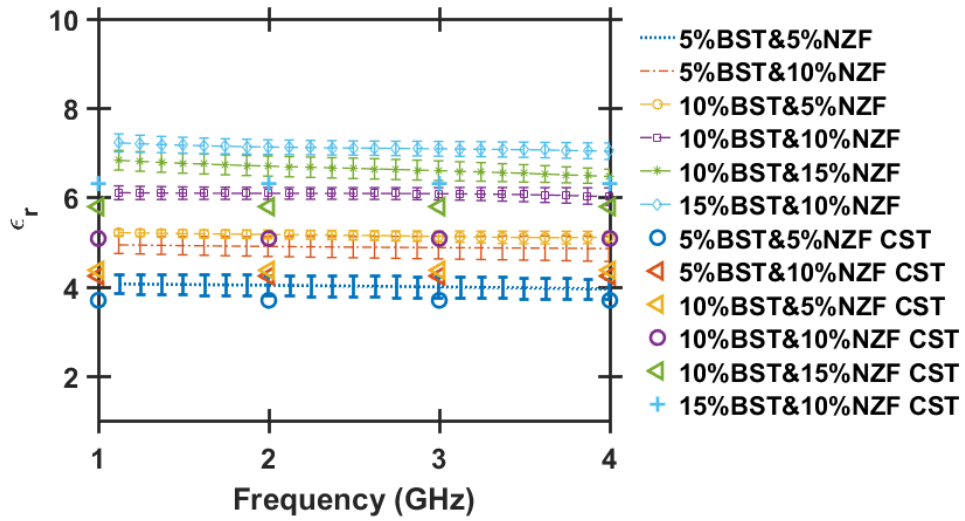

Figure 31. Effective real permittivity for various fractions of combined BST and NZF mixing composites. The lines with error bars are from measurements and the symbols from CST simulations.

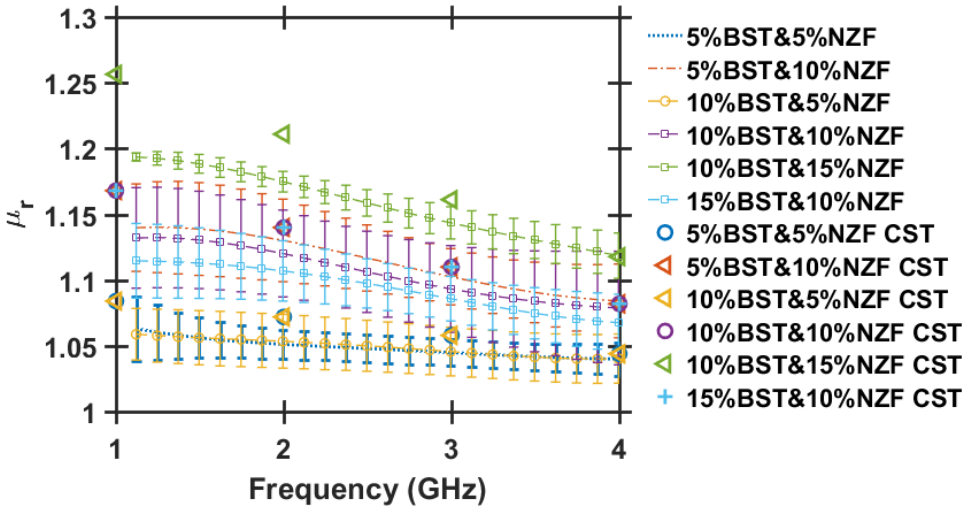

Figure 32. Effective real permeability for various fractions of combined BST and NZF mixing composites. The lines with error bars are from measurements and the symbols from CST simulations.

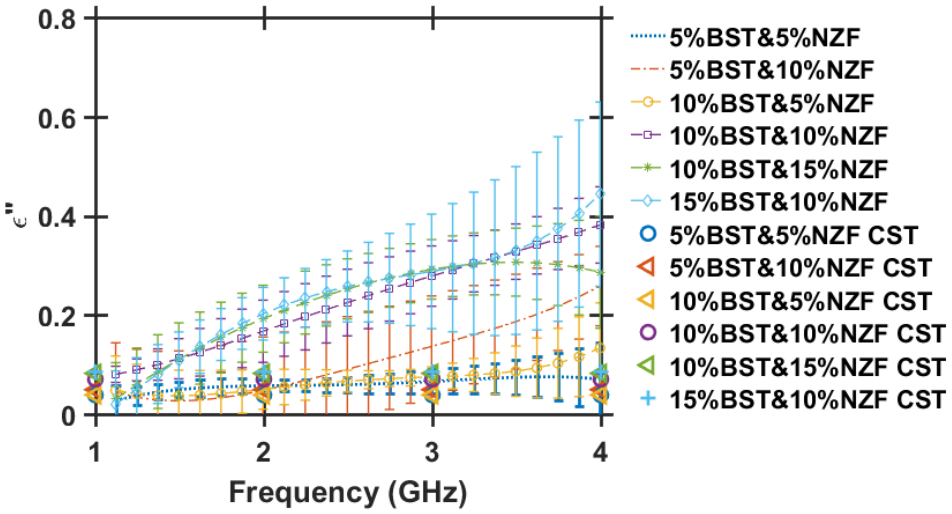

Figure 33. Effective imaginary permittivity for various fractions of combined BST and NZF mixing composites. The lines with error bars are from measurements and the symbols from CST simulations.

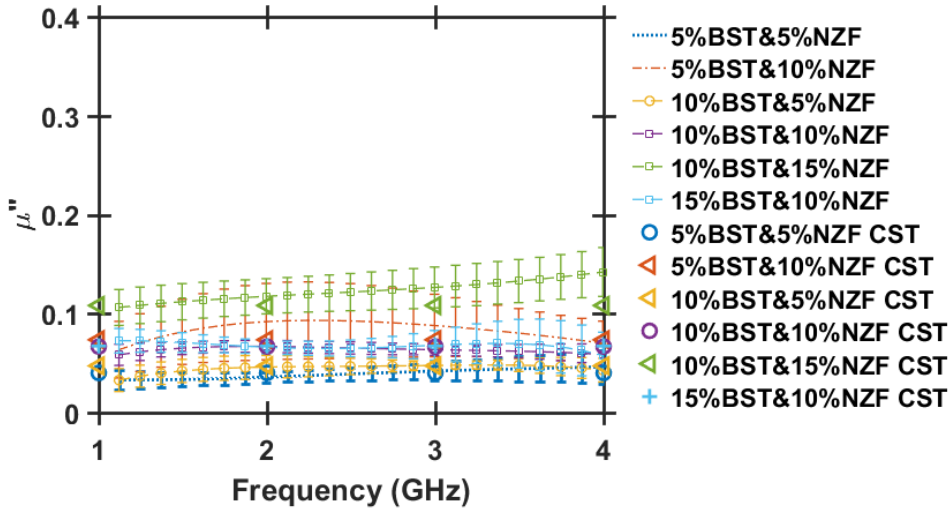

Figure 34. Effective imaginary permeability for various fractions of combined BST and &NZF mixing composites with various volume fractions. The lines with error bars are from measurements and the symbols from CST simulations.

Despite the lower estimates for the effective real permittivity from the models, the effective real permittivity depends more strongly on the total volume loading. However, BST inclusions still contribute more to the effective permittivity than NZF inclusions, as shown

in Figure 35. Moreover, Figure 36 shows that the effective permeability of the combined BST and NZF composites depends only on the volume fraction of the NZF inclusions because BST is nonmagnetic.

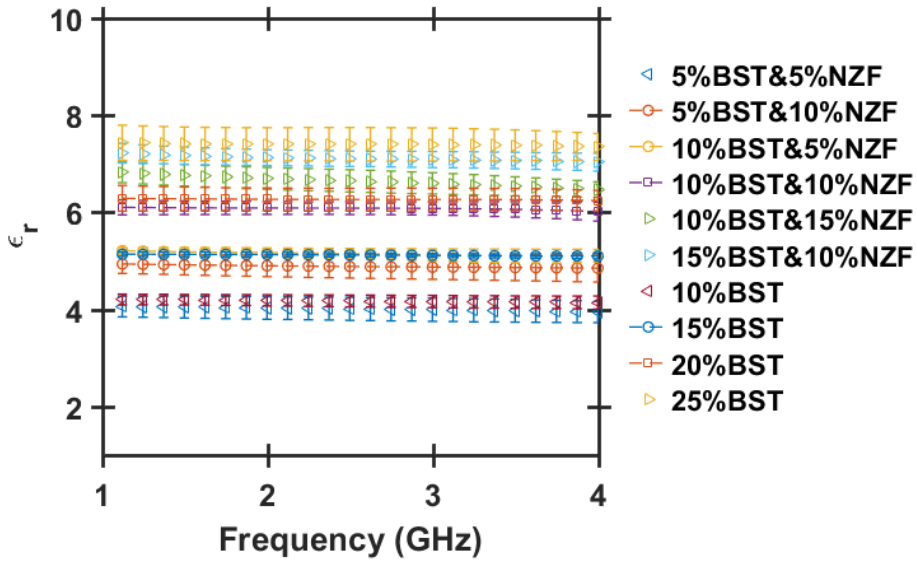

Figure 35. Assessment of effective real permittivity for different total volume fractions of combined BST and NZF composites and BST composites.

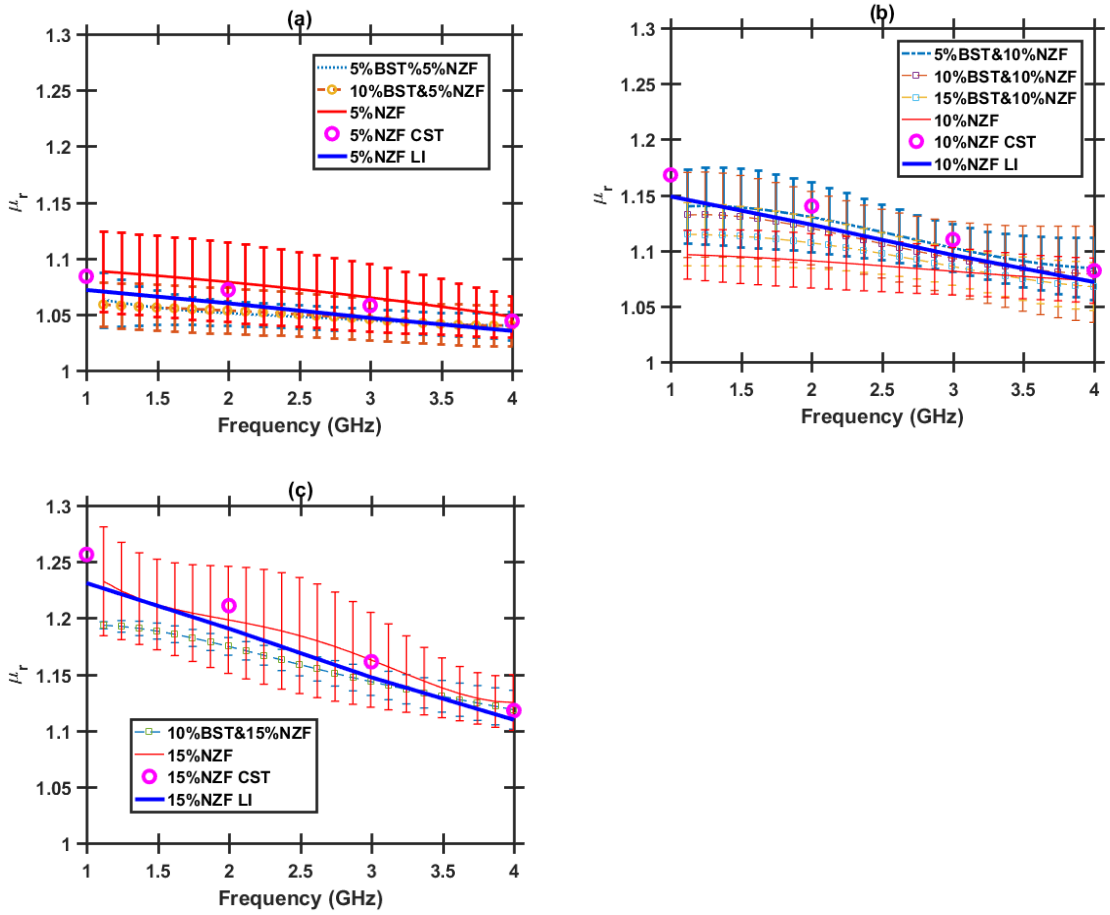

Figure 36. Effective real permeability μ_r of combined BST and NZF composites and NZF composites NZF volume loadings of (a) 5% NZF, (b) 10% NZF, (c) 15% NZF. Also included are μ_r for the NZF composite alone determined experimentally and using CST simulation or the Lichtenecker rule (LI). The permeability depends solely on the permeability of NZF since BST is nonmagnetic.

6. CONCLUSIONS AND FUTURE WORK

This thesis assessed various classical effective medium theories (EMTs) and developed a simulation approach in CST Microwave Studio (CST MWS) in the quasi-static limit for calculating the effective complex permittivity and permeability of nonlinear composites in linear region (for a fixed low voltage and current). The CST MWS composite models build upon the advancements made in recent simulation and theoretical works [45], [47].

The nonlinear composites are comprised of a polymer base dielectric PDMS with nonlinear dielectric inclusions barium strontium titanate (BST) and/or nonlinear magnetic inclusions nickel zinc ferrites (NZF). The ultimate goal of the overall research project is to investigating the tuning of the effective permittivity and permeability of the nonlinear composite by manipulating the volume loading of the nonlinear inclusions. The nonlinear composites will be used in the future designs of novel nonlinear transmission lines (NLTLs) to provide additional flexibility in design and potentially increase efficiency and energy in the RF output, as detailed in Chapter 1.

The homogeneity of the composites is vital for applying the EMTs and CST MWS to predict the effective dielectric properties, as detailed in Chapter 2. We manufactured the nonlinear composites with specific procedures for ensuring the homogeneous distributions of the inclusions and performed 3D X-ray scans to show the homogeneity of the composite samples. Except for a few aggregations of inclusions with sufficiently small sizes according to the quasi-static limit, the inclusions may generally be considered homogeneously distributed. Various volume fractions were considered for the composite manufacturing,

including BST, NZF and BST&NZF composites, as shown in Table 2. Then, the effective dielectric properties (complex permittivity and permeability) of the composites were measured by using a network analyzer in linear region (power -15 dBm, voltage 40 mV), as introduced in Chapter 3.

Because we currently do not have reliable data for the bulk conductivity of the BST and NZF inclusions between 1 and 4 GHz, we fit the classical EMTs to our composite measurements to estimate the bulk dielectric properties of the BST and NZF inclusions to use inputs in the composite simulations in CST MWS. However, this method only works for the real permittivity and permeability of NZF; the anticipated conductivities of BST and NZF were too low to account for the observed imaginary permittivity and permeability. Based on these estimates and literature values, the classical EMTs seem limited to cases where the volume loading of inclusions is low or the electrical contrast is not too great, as detailed in Chapter 4.

The imaginary permittivity and permeability of NZF from the measurements in Ref. [84], [86] at 1 GHz were used in the NZF composite models as starting points for tuning the inputs in CST MWS to match with our composite measurements, although the compositions of their NZF samples might be different from that of ours. Setting $\tan\delta$ = 0.06 and $\tan\delta_m$= 0.5 for NZF at 1 GHz gave the best fit with the composite measurements in terms of order of magnitude. We have not yet successfully predicted the dispersions of the imaginary permittivity and permeability of NZF composites from 1 to 4 GHz due to

poor simulation efficiency. We encountered the same challenge when assessing the imaginary permittivity of BST composites.

Two measurements of BST ($Ba_{2/3}Sr_{1/3}TiO_3$) at different frequencies (500 MHz and 1 GHz) reported the same real permittivity data [82], [83]. By assuming there is no frequency dispersion ranging from 500 MHz to 1 GHz and considering the same composition of BST, we applied this value with its corresponding loss tangent in the BST composite models for current assessments. The resulting effective permittivity with this input and subsequent results with tuned values ranging from 1500 to 2500 are all lower than the measurements, as shown in Table 4. This may indicate that the actual value of the real permittivity of BST is much higher than the input we used.

The current simulation conditions and mesh settings limit the tuning approach in CST MWS to estimate the real permittivity of BST and the dispersions of the imaginary permittivity and permeability of both BST and NZF. We have not yet successfully set local mesh properties for different potions in the model to reduce mesh cells. The unified mesh size in the rectangular composite bulk considerably limits the simulation efficiency and the accuracy of the models, as detailed in Chapter 4.

Based on the estimates from the classical EMTs, tuned values, and literature data, the NZF, BST and BST&NZF composite models in CST MWS were performed for various volume fractions and the results were compared with the composite measurements, as detailed in Chapter 5.

The NZF composite models generally agree well with measurements and the Lichtenecker rule for the real permittivity and permeability ranging from 1 to 4 GHz. Though the inputs of the electrical and magnetic loss tangent were obtained from tuning the NZF composite models and not verified by measurements, the CST MWS models are still able to give reasonable fit on the orders of magnitude for the imaginary permittivity and permeability of NZF, permitting to assess the losses of the NLTLs comprised of the nonlinear composites at a certain frequency.

Although the BST composite models underestimated the effective real permittivity by applying the literature value, they still agree with the composite measurements better than the classical EMTs, as illustrated in Figure 30. Also, by using the corresponding loss tangent at 500 MHz, the BST models can reasonably estimate the electrical losses for different volume fractions except for the dispersions at higher frequencies.

The combined BST and NZF composite models agree well with measurements and the LI rule for the effective real permeability, although they underestimate the effective real permittivity, similar to our observations above for the BST only composites. Again, this may arise due to BST actually possessing a higher real permittivity or due to factors not currently considered in our theory or simulation.

In summary, the classical EMTs specifically the LI rule and CST MWS composite models can estimate the dielectric properties with low electric contrast. For the cases with strong

electric contrast, CST MWS models provide better estimations than the classical EMTs. Better assessments for the effective real permittivity BST and BST&NZF composites and the dispersions for the imaginary permittivity and permeability require measurements of the dielectric and magnetic properties of the BST and NZF inclusions.

Future work will measure the dielectric properties of BST and NZF at 1~4 GHz to benchmark the composite models in CST MWS. The mesh settings, such as the local mesh properties of inclusions, must be improved to increase the simulation performance. The validity of the quasi-static limit will be testified by varying the sizes of the inclusions. Further simulations may use smaller size of the inclusions to improve the homogeneity of the composite models and the quasi-static limit.

Ultimately, successfully benchmarking the spherical model to experimental data in CST MWS will permit us to effectively assess the impact of inclusion shape and orientation for non-spherical inclusions. A valid simulation tool also allows assessing the exponents *s* and *t* in the GEMT, which may provide another avenue for accurately predicting the effective properties [37], [79]. Based on these concepts, we may develop nonlinear EMTs to describe the dielectric ($\varepsilon_{eff}(f,V)$) and magnetic ($\mu_{eff}(f,I)$) properties of the nonlinear composites for guiding future NLTLs designs.

Understanding the nonlinear behavior of the effective dielectric and magnetic properties of the nonlinear composites permits properly tailoring the functions of *C*(*f, V*) and *L*(*f, I*) for pulse sharpening and high-power RF generation in nonlinear hybrid lines (NLHLs) [3],

[32]–[36]. Although one study has applied circuit modeling to a nonlinear hybrid lumped element transmission line at 50-70 MHz [32], a full, multiscale model starting from the development of the transmission line properties to the generation of RF has not been designed, particularly at higher operating frequency [3]. Gyromagnetic NLTLs appear to be more effective at achieving signals at several GHz with peak power of tens of MW for HPM generation [3]. However, applying gyromagnetic precession for HPM generation by using nonlinear composites containing NZF powders requires not only predicting the nonlinear behavior of composites but also characterizing the precessional motion of magnetization when nonlinear composites saturate [1], [25]–[27].

REFERENCES

[1] J.-W. B. Bragg, J. C. Dickens, and A. A. Neuber, “Ferrimagnetic nonlinear transmission lines as high-power microwave sources,” *IEEE Trans. Plasma Sci.*, vol. 41, no. 1, pp. 232–237, Jan. 2013.

[2] J. Gaudet, E. Schamiloglu, J. O. Rossi, C. J. Buchenauer, and C. Frost, “Nonlinear transmission lines for high power microwave applications - a survey,” in *Proc. 28th IEEE Int. Power Mod. Conf./High Voltage Workshop*, Las Vegas, NV, 2008, pp. 131–138.

[3] J. O. Rossi, L. P. Silva Neto, F. S. Yamasaki, and J. J. Barroso, “State of the art of nonlinear transmission lines for applications in high power microwaves,” in *Proc. SBMO/IEEE MTT-S IMOC*, Rio de Janeiro, Brazil, Aug. 2013, pp. 1–5.

[4] J. A. Schrock, B. W. Hoff, D. H. Simon, S. L. Heidger, P. Lepell, J. Gilbrech, H. Wood, and R. Richter-sand. “Spatially dispersive nonlinear transmission line experimental performance analysis,” *IEEE Trans. Dielectr. Electr. Insul.*, vol. 26, no. 2, pp. 412–415, Apr. 2019.

[5] J. O. Rossi, L. P. Silva, J. J. Barroso, F. S. Yamasaki, and E. Schamiloglu, “Overview of RF generation using nonlinear transmission lines,” in *Proc. 25th IEEE Int. Pulsed Power Conf.* Austin, TX, USA, May/Jun. 2015, pp. 1–6.

[6] E. Afshari and A. Hajimiri, “Nonlinear transmission lines for pulse shaping in silicon,” *IEEE J. Solid-State Circuits*, vol. 40, no. 3, pp. 744–752, Mar. 2005.

[7] E. Afshari, H. S. Bhat, A. Hajimiri, and J. E. Marsden, “Extremely wideband signal shaping using one- and two-dimensional nonuniform nonlinear transmission lines,” *J. Appl. Phys.*, vol. 99, Mar. 2006, Art. no. 054901.

[8] L. P. S. Neto, J. O. Rossi, J. J. Barroso, and E. Schamiloglu, “Hybrid nonlinear transmission lines used for RF soliton generation,” *IEEE Trans. Plasma Sci.*, vol. 46, no. 10, pp. 3648–3652, Oct. 2018.

[9] P. W. Smith, *Transient Electronics: Pulsed Circuit Technology*. New York, UNITED KINGDOM: John Wiley & Sons, Incorporated, 2002.

[10] J. O. Rossi and P. N. Rizzo, “Study of hybrid nonlinear transmission lines for high power RF generation,” in *Proc. IEEE Int. Pulsed Power Conf.*, Washington, DC, USA, Jun./Jul. 2009, pp. 46–50.

[11] K. G. Lyon and E. C. Kan, “Microwave pulse generation using the Bragg cutoff of a nonlinear transmission line,” in *Microwave Symposium, 2008. IEEE/MTT-S Int.*, June, 2008.

[12] J. D. Darling and P. W. Smith, “High power RF generation from non-linear delay lines,” in *Proc. IEEE 34th Int. Conf. on Plasma Sci.* Albuquerque, NM, USA, Jun. 2007, pp. 472–475.

[13] J. D. Darling and P. W. Smith, “High power pulse burst generation by soliton-type oscillation on nonlinear lumped element transmission lines,” in *Proc. 2009 IEEE Pulsed Power Conf.*, pp. 119-123, June 2009.

[14] M. M. Turner, G. Branch, and P. W. Smith, “Methods of theoretical analysis and computer modeling of the shaping of electrical pulses by nonlinear transmission lines and lumped-element delay lines,” *IEEE Trans. Electron Devices*, vol. 38, no. 4, pp. 810–816, Apr. 1991.

[15] E. Stenglein and M. Albach, “Analytical calculation method for the non-linear characteristic of ferrite-cored inductors with stepped air gap,” *Electr. Eng.*, vol. 99, no. 1, pp. 421–429, Mar. 2017.

[16] F. S. Yamasaki, L. P. S. Neto, J. O. Rossi, and J. J. Barroso, “Soliton generation using nonlinear transmission lines,” *IEEE Trans. Plasma Sci.*, vol. 42, no. 11, pp. 3471–3477, Nov. 2014.

[17] N. S. Kuek, A. C. Liew, E. Schamiloglu, and J. O. Rossi, “Pulsed RF oscillations on a nonlinear capacitive transmission line,” *IEEE Trans. Dielectr. Electr. Insul.*, vol. 20, no. 4, pp. 1129–1135, Aug. 2013.

[18] L. P. Silva Neto, J. O. Rossi, J. J. Barroso, and E. Schamiloglu, “High-power RF generation from nonlinear transmission lines with barium titanate ceramic capacitors,” *IEEE Trans. Plasma Sci.*, vol. 44, no. 12, pp. 3424–3431, Dec. 2016.

[19] J. Bragg, J. Dickens, and A. Neuber, “Magnetic biasing of ferrite filled nonlinear transmission lines,” in *Proc. 2010 Power Modulator and HV Conf.*, Atlanta, GA, pp. 600-603, May 2010.

[20] V. V. Rostov, N. M. Bykov, D. N. Bykov, A. I. Klimov, O. B. Kovalchuk, and I. V. Romanchenko, “Generation of subgigawatt rf pulses in nonlinear transmission lines,” *IEEE Trans. Plasma Sci.*, vol. 38, no. 10, pp. 2681–2685, Oct. 2010.

[21] I. V. Romanchenko, V. V. Rostov, V. P. Gubanov, A. S. Stepchenko, A. V. Gunin, and I. K. Kurkan, “Repetitive sub-gigawatt RF source based on gyromagnetic nonlinear transmission line,” *Rev. Sci. Instrum.*, vol. 83, no. 7, pp. 074705-1-074705-6, 2012.

[22] S. J. F. Chadwick, N. Seddon, and S. Rukin, “A novel solid-state HPM source based on a gyromagnetic NLTL and SOS-based pulse generator,” in *Proc.18th IEEE Int. Pulsed Power Conf.*, Chicago, IL, pp. 178-181, June 2011.

[23] F. S. Yamasaki, J. O. Rossi, J. J. Barroso, and E. Schamiloglu, “Operation of a gyromagnetic line at low and high voltages with simultaneous axial and azimuthal biases,” *IEEE Trans. Plasma Sci.*, vol. 46, no. 7, pp. 2573–2581, Jul. 2018.

[24] J.-W. B. Bragg, W. W. Sullivan, D. Mauch, A. A. Neuber, and J. C. Dickens, “All solid-state high power microwave source with high repetition frequency,” *Rev. Sci. Instrum.*, vol. 84, no. 5, May 2013, Art. no. 054703.

[25] D. V. Reale, “Coaxial ferrimagnetic based gyromagnetic nonlinear transmission lines as compact high power microwave sources,” Ph. D. dissertation, Dept. Elect. Eng., Texas Tech Univ., Lubbock, TX, Dec. 2013.

[26] T. L. Gilbert, “Classics in magnetics a phenomenological theory of damping in ferromagnetic materials,” *IEEE Trans. Magn.*, vol. 40, no. 6, pp. 3443–3449, Nov. 2004.

[27] J.-W. B. Bragg, J. C. Dickens, and A. A. Neuber, “Material selection considerations for coaxial, ferrimagnetic-based nonlinear transmission lines,” *J. Appl. Phys.*, vol. 113, no. 6, 2013, Art. no. 064904.

[28] D. V. Reale, J.-W. B. Bragg, N. R. Gonsalves, J. M. Johnson, A. A. Neuber, J. C. Dickens, and J. J. Mankowski, “Bias-field controlled phasing and power combination of gyromagnetic nonlinear transmission lines,” *Rev. Sci. Instrum.*, vol. 85, no. 5, May 2014, Art. no. 054706.

[29] H. Ikezi, J. S. DeGrassie, and J. Drake, “Soliton generation at 10 MW level in the very high frequency band,” *Appl. Phys. Lett.*, vol. 58, no. 9, pp. 986–987, Mar. 1991.

[30] H. Ikezi, S. S. Wojtowicz, R. E. Waltz, and D. R. Baker, “Temporal contraction of solitons in a nonuniform transmission line,” *J. Appl. Phys.*, vol. 64, no. 12, pp. 6836–6838, Dec. 1988.

[31] D. M. French, B. W. Hoff, S. Heidger, and D. Shiffler, “Dielectric nonlinear transmission line,” in *Proc. 18th IEEE Int. Pulsed Power Conf.*, Chicago, IL, USA, 2011, pp. 341–345.

[32] N. S. Kuek, A. C. Liew, E. Schamiloglu, and J. O. Rossi, “Circuit modeling of nonlinear lumped element transmission lines including hybrid lines,” *IEEE Trans. Plasma Sci.*, vol. 40, no. 10, pp. 2523–2534, Oct. 2012.

[33] F. Fallside and D. T. Bickley, “Nonlinear delay line with a constant characteristic impedance,” *Proc. Inst. Electr. Eng.*, vol. 113, no. 2, pp. 263–270, Feb. 1966.

[34] J. O. Rossi, P. N. Rizzo, and F. S. Yamasaki, “Prospects for applications of hybrid lines in RF generation,” in *Proc. 2010 IEEE Int. Power Modulator and HV Conf.*, Atlanta, pp. 632–635, May 2010.

[35] O. S. F. Zucker and W. H. Bostick, “Theoretical and practical aspects of energy storage and compression,” in *Energy Storage*, *Compression and Switching*, W. H. Bostick, V. Nardi, and O. S. F. Zucker, Eds. New York: Plenum, 1976, pp. 71–93.

[36] N. S. Kuek, A. C. Liew, E. Schamiloglu, and J. O. Rossi, “RF pulse generator based on a nonlinear hybrid line,” *IEEE Trans. Plasma Sci.*, vol. 42, no. 10, pp. 3268–3273, Oct. 2014.

[37] A. L. Garner, G. J. Parker, and D. L. Simone, “A semi-empirical approach for predicting the performance of multiphase composites at microwave frequencies,” *IEEE Trans. Dielectr. Electr. Insul.*, vol. 23, no. 2, pp. 1126–1134, Apr. 2016.

[38] A. L. Garner, G. J. Parker, and D. L. Simone, “Predicting effective permittivity of composites containing conductive inclusions at microwave frequencies,” *AIP Adv.*, vol. 2, Sep. 2012, Art. no. 032109.

[39] Y. Wu, Y. Lai, and Z.-Q. Zhang, “Effective medium theory for elastic metamaterials in two dimensions,” *Phys. Rev. B*, vol. 76, Nov. 2007, Art. no. 205313.

[40] F. Qin and C. Brosseau, “A review and analysis of microwave absorption in polymer composites filled with carbonaceous particles,” *J. Appl. Phys.*, vol. 111, Mar. 2012, Art. no. 061301.

[41] T. Galek, K. Porath, E. Burkel, and U. van Rienen, “Extraction of effective permittivity and permeability of metallic powders in the microwave range,” *Model. Simul. Mater. Sci. Eng.*, vol. 18, Mar. 2010, Art. no. 025015.

[42] A. H. Sihvola, *Electromagnetic Mixing Formulas and Applications*. London, U.K.: IET, 1999.

[43] K. Zhou and S. Boggs, “Effective dielectric constant of a linear matrix filled with linear and nonlinear spherical particles,” in *2009 IEEE Pulsed Power Conf.*, Washington, DC, USA, 2009, pp. 342–345.

[44] K. A. O’Connor and R. D. Curry, “Three-dimensional electromagnetic modeling of composite dielectric materials,” in *2011 IEEE Pulsed Power Conf.*, Chicago, IL, USA, 2011, pp. 274–279.

[45] C. Baer, B. Hattenhorst, C. Schulz, B. Will, I. Rolfes, and T. Musch, “Effective permittivity determination of randomized mixed materials using 3D electromagnetic simulations,” in *2015 IEEE MTT-S International Microwave Symposium*, Phoenix, AZ, USA, 2015, pp. 1–4.

[46] O. Rybin and S. Shulga, “Advanced microwave effective medium theory for two-component nonmagnetic metamaterials: fundamentals and antenna substrate application,” *J. Comput. Electron.*, vol. 16, no. 2, pp. 369–381, Jun. 2017.

[47] X. Chen, T. M. Grzegorczyk, B.-I. Wu, J. Pacheco, and J. A. Kong, “Robust method to retrieve the constitutive effective parameters of metamaterials,” *Phys. Rev. E*, vol. 70, Jul. 2004, Art. no. 016608.

[48] P. Kim, N. M. Doss, J. P. Tillotson, P. J. Hotchkiss, M.-J. Pan, and S. R. Marder, J. Li, J. P. Calame, and J. W. Perry, “High energy density nanocomposites based on surface-modified $BaTiO_3$ and a ferroelectric polymer,” *ACS Nano*, vol. 3, no. 9, pp. 2581–2592, Sep. 2009.

[49] D. M. Pozar, *Microwave Engineering*. 2nd Ed., Toronto: John Wiley & Sons, 1998.

[50] O. G. Martinsen, S. Grimnes, *Bioimpedance and Bioelectricity Basics*. London, UK: Academic, 2000.

[51] T. Tsutaoka, “Frequency dispersion of complex permeability in Mn–Zn and Ni–Zn spinel ferrites and their composite materials,” *J. Appl. Phys.*, vol. 93, pp. 2789-2796, 2003.

[52] G. T. Rado, R. W. Wright, and W. H. Emerson, “Ferromagnetism at very high frequencies. iii. two mechanisms of dispersion in a ferrite,” *Phys. Rev.*, vol. 80, no. 2, pp. 273–280, Oct. 1950.

[53] T. Tsutaoka, H. Sugitani, T. Kasagi, and K. Hatakeyama, “Magnetic field effect on the permeability of Mn-Zn ferrite composite materials,” *J. Magn. Soc. Jpn.*, vol. 25, pp. 943–946, Jan. 2001.

[54] L. Jylhä and A. Sihvola, “Equation for the effective permittivity of particle-filled composites for material design applications,” *J. Phys. Appl. Phys.*, vol. 40, no. 16, pp. 4966–4973, Aug. 2007.

[55] J. C. Maxwell Garnett, “Colours in metal glasses and in metallic films”, Philos. Trans. R. Soc., London, Ser. A., vol. 203, pp. 385-420, 1904.

[56] D. A. G. Bruggeman, “Calculation of various physics constants in heterogeneous substances I Dielectric constants and conductivity of mixed bodies from isotropic substances,” *Ann. Phys*., vol. 24, no. 7, pp. 636-664, 1935.

[57] H. Fricke, “A mathematical treatment of the electric conductivity and capacity of disperse systems ii. the capacity of a suspension of conducting spheroids surrounded by a non-conducting membrane for a current of low frequency,” *Phys. Rev.*, vol. 26, no. 5, pp. 678–681, Nov. 1925.

[58] H. Fricke, “The Maxwell-Wagner dispersion in a suspension of ellipsoids,” *J. Phys. Chem.*, vol. 57, no. 9, pp. 934–937, Sep. 1953.

[59] V. A. Markel, “Introduction to the Maxwell Garnett approximation: tutorial,” *J. Opt. Soc. Amer. A, Opt. Image Sci.*, vol. 33, no. 7, pp. 1244–1256, 2016.

[60] H. Looyenga, “Dielectric constants of heterogeneous mixtures,” *Physica*, vol. 31, no. 3, pp. 401–406, Mar. 1965.

[61] K. Lichtenecker, “Dielectric constant of natural and synthetic mixtures,” *Phys Z*, vol. 27, pp. 115-158, 1926.

[62] R. Simpkin, “Derivation of Lichtenecker’s logarithmic mixture formula from Maxwell’s equations,” *IEEE Trans. Microw. Theory Tech.*, vol. 58, no. 3, pp. 545–550, Mar. 2010.

[63] T. Zakri, J.-P. Laurent, and M. Vauclin, “Theoretical evidence for `Lichtenecker’s mixture formulae’ based on the effective medium theory,” *J. Phys. Appl. Phys.*, vol. 31, no. 13, pp. 1589–1594, Jul. 1998.

[64] M. H. Boyle, “The electrical properties of heterogeneous mixtures containing an oriented spheroidal dispersed phase,” *Colloid Polym. Sci.*, vol. 263, no. 1, pp. 51–57, Jan. 1985.

[65] S. Giordano, “Effective medium theory for dispersions of dielectric ellipsoids,” *J. Electrost.*, vol. 58, no. 1–2, pp. 59–76, May 2003.

[66] J. W. Haus, R. Inguva, and C. M. Bowden, “Effective-medium theory of nonlinear ellipsoidal composites,” *Phys. Rev. A*, vol. 40, no. 10, pp. 5729–5734, Nov. 1989.

[67] S. Berthier, “Anisotropic effective medium theories,” *J. Phys. I*, vol. 4, no. 2, pp. 303–318, Feb. 1994.

[68] P. A. Fokker, “General anisotropic effective medium theory for the effective permeability of heterogeneous reservoirs,” *Transp. Porous Media*, vol. 44, no. 2, pp. 205–218, Aug. 2001.

[69] D. S. McLachlan, “An equation for the conductivity of binary mixtures with anisotropic grain structures,” *J. Phys. C Solid State Phys.*, vol. 20, no. 7, pp. 865–877, Mar. 1987.

[70] C. Brosseau, “Generalized effective medium theory and dielectric relaxation in particle-filled polymeric resins,” *J. Appl. Phys.*, vol. 91, no. 5, pp. 3197–3204, Mar. 2002.

[71] C. Chiteme and D. S. McLachlan, “AC and DC conductivity, magnetoresistance, and scaling in cellular percolation systems,” *Phys. Rev. B*, vol. 67, Jan. 2003, Art. no. 024206.

[72] A. L. Garner, G. J. Parker, and D. L. Simone, “Accounting for conducting inclusion permeability in the microwave regime in a modified generalized effective medium theory,” *IEEE Trans. Dielectr. Electr. Insul.*, vol. 22, no. 4, pp. 2064–2072, Aug. 2015.

[73] B. Bianco and M. Parodi, “A unifying approach for obtaining closed-form expressions of mixtures permittivity,” *J. Electrost.*, vol. 15, no. 2, pp. 183–195, Jun. 1984.

[74] B. Sareni, L. Krähenbühl, A. Beroual, and C. Brosseau, “Effective dielectric constant of periodic composite materials,” *J. Appl. Phys.*, vol. 80, no. 3, pp. 1688–1696, Aug. 1996.

[75] B. Sareni, L. Krähenbühl, A. Beroual, and C. Brosseau, “Effective dielectric constant of random composite materials,” *J. Appl. Phys.*, vol. 81, no. 5, pp. 2375–2383, Mar. 1997.

[76] V. Myroshnychenko and C. Brosseau, “Finite-element method for calculation of the effective permittivity of random inhomogeneous media,” *Phys. Rev. E*, vol. 71, Jan. 2005, Art. no. 016701.

[77] V. Myroshnychenko and C. Brosseau, “Finite-element modeling method for the prediction of the complex effective permittivity of two-phase random statistically isotropic heterostructures,” *J. Appl. Phys.*, vol. 97, Feb. 2005, Art. no. 044101.

[78] V. Myroshnychenko and C. Brosseau, “Effective complex permittivity of two-phase random composite media: A test of the two exponent phenomenological percolation equation,” *J. Appl. Phys.*, vol. 103, Apr. 2008, Art. no. 084112.

[79] V. Myroshnychenko and C. Brosseau, “Possible manifestation of nonuniversality in some continuum percolation systems,” *J. Phys. Appl. Phys.*, vol. 41, Apr. 2008, Art. no. 095401.

[80] J. Baker-Jarvis, E. J. Vanzura, and W. A. Kissick, “Improved technique for determining complex permittivity with the transmission/reflection method,” *IEEE Trans. Microw. Theory Tech.*, vol. 38, no. 8, pp. 1096–1103, Aug. 1990.

[81] A. M. Nicolson and G. F. Ross, “Measurement of the Intrinsic Properties of Materials by Time-Domain Techniques,” *IEEE Trans. Instrum. Meas.*, vol. 19, no. 4, pp. 377–382, Nov. 1970.

[82] K. Nadaud, C. Borderon, R. Renoud, A. Ghalem, A. Crunteanu, L. Huitema, F. Dumas-Bouchiat, P. Marchet, C. Champeaux, and H. W. Gundel “Effect of the incident power on permittivity, losses and tunability of $BaSrTiO_3$ thin films in the microwave frequency range,” *Appl. Phys. Lett.*, vol. 110, May 2017, Art. no. 212902.

[83] A. Ghalem, M. Rammal, and A. Crunteanu, “Ultra-high tunability $Ba_{(2/3)}Sr_{(1/3)}TiO_3$-based capacitors under low electric fields,” *IEEE Microw. Wirel. Compon. Lett.*, vol. 26, no. 7, pp. 504–506, Jul. 2016.

[84] J. C. Aphesteguy, A. Damiani, D. DiGiovanni, and S. E. Jacobo, “Microwave-absorbing characteristics of epoxy resin composites containing nanoparticles of NiZn- and NiCuZn-ferrites,” *Phys. B Condens. Matter*, vol. 404, no. 18, pp. 2713–2716, Oct. 2009.

[85] L. Chao, A. Sharma, M. N. Afsar, O. Obi, Z. Zhou, and N. Sun, "Permittivity and permeability measurement of spin-spray deposited Ni-Zn-ferrite thin film sample," *IEEE Trans. Magn.*, vol. 48, no. 11, pp. 4085–4088, Nov. 2012.

[86] A. C. Razzitte, W. G. Fano, and S. E. Jacobo, "Electrical permittivity of Ni and NiZn ferrite–polymer composites," *Phys. B Condens. Matter*, vol. 354, no. 1, pp. 228–231, Dec. 2004.

[87] T. Delage, C. Champeaux, A. Catherinot, J. F. Seaux, V. Madrangeas, and D. Cros, "High-K BST films deposited on MgO by PLD with and without buffer-layer," *Thin Solid Films*, vol. 453–454, pp. 279–284, Apr. 2004.

[88] M. P. Reddy, G. Kim1, D. S. Yoo, W. Madhuri, N. R. Reddy, K. V. S. Kumar, and R. R. Reddy, "Characterization and electromagnetic studies on NiZn and NiCuZn ferrites prepared by microwave sintering technique," *Mater. Sci. Appl.*, vol. 03, no. 9, pp. 628–632, 2012.

[89] P. Yadoji, R. Peelamedu, D. Agrawal, and R. Roy, "Microwave sintering of Ni–Zn ferrites: comparison with conventional sintering," *Mater. Sci. Eng. B*, vol. 98, no. 3, pp. 269–278, Apr. 2003.

[90] J. W. Liou and B. S. Chiou, "Dielectric tunability of barium strontium titanate/silicone-rubber composite," *J. Phys. Condens. Matter*, vol. 10, no. 12, pp. 2773–2786, Mar. 1998.

[91] *Material Property Database.* Accessed on: Oct. 29, 2019, [Online], Available: http://www.mit.edu/~6.777/matprops/pdms.htm

[92] *Ferrite Powders-Inductive & EMI Shielding Applications- Valparaiso, Indiana*. Accessed on: Oct. 29, 2019 [Online]. Available: https://www.pptechnology.com/electronic-soft-ferrite-powders.html

[93] *HBS-8000, 500-900 nm Barium Strontium Titanate.* [Online]. Available: http://www.tplinc.com/uploads/HBS-8000_Technical_Bulletin.pdf

[94] B.-I. Wu, W. Wang, J. Pacheco, X. Chen, T. M. Grzegorczyk, and J. A. Kong, "A study of using metamaterials as antenna substrate to enhance gain," *Prog. Electromagn. Res.*, vol. 51, pp. 295–328, 2005.

VITA

Education:

Master of science, Nuclear Engineering, Purdue University, West Lafayette, IN. Anticipated 12/19
Thesis Title: *Assessing Effective Medium Theories for Designing Composites for Nonlinear Transmission Lines*.
Advisor: Allen L. Garner

Bachelor of science, Applied Physics, Chengdu University of Technology, Sichuan, China. 06/16

Research Experience:

BioElectrics and ElectroPhysics Laboratory (BEEP), Purdue University 08/18-present
Research Assistant under Prof. Allen Garner

- Simulations of novel nonlinear composites by using effective medium theories (EMTs) and CST Microwave Studio for novel nonlinear transmission lines (NLTLs) design for high-power microwave (HPM) generation.
- Modeling of pulse sharpening and microwave generation using NLTLs

Center for Materials Under Extreme Environment (CMUXE), Purdue University 01/18-07/18
Advisor: Prof. Tatyana Sizyuk

- Simulated helium diffusion, helium bubble formation and fuzzy nanostructure formation in fusion material tungsten by using Molecular Dynamics.
- Investigated laser ablation and phase explosion of aluminum and silicon by using Monte Carlo method.

Department of Applied Physics, Chengdu University of Technology, China 10/13-03/15
Advisor: Prof. Bangling Deng

- Simulated atomic parameters for Kα X-ray from He-like to Ne-like phosphorus using the multi-configuration Dirac-Fock, relativistic configuration interaction methods and GRASPVU programming package.

Relevant Skills:

- CST Microwave Studio for microwave applications
- MATLAB, Mathematica
- Fortran and Python for computational physics applications
- GRASPVU programming package for atomic parameters calculations

Conference Oral Presentations [*italics*=presenter]

1. ***X. Zhu***, A. J. Fairbanks, and A. L. Garner, "Assessing Effective Medium Theories for Designing Composites for Nonlinear Transmission Lines," IEEE Pulsed Power and Plasma Science Conference, 2C2, 24 June 2019.
2. *A. Fairbanks*, **X. Zhu**, J. Hernandez, S. Gao, W. Wu, T. Tallman, and A. Garner,

"Development and Diagnostics on Composites for Nonlinear Transmission Lines," IEEE Pulsed Power and Plasma Science Conference, 2C3, 24 June 2019.

Refereed Journal Articles

- **X. J. Zhu**, B. L. Deng, C. Y. Zhang, S. P. Shi, & G. Jiang. "Calculations of relativistic configuration interaction for Kα X-ray satellites of phosphorus ions". *Indian Journal of Physics*, 90(2), 225-231(2016).

Professional Organizations:

- **IEEE** Student Member 2019-

Awards:

- China National Scholarship (Granted by Ministry of Education of China) 2015
- Excellent Graduate of Sichuan Province (Granted by Education Department in Sichuan) 2016